Device and Process Design for Hydraulic Microfluidics

by

Michael L. Vladimer

A research project submitted in partial fulfillment of the requirements for the degree of

Master of Science

in

Electrical & Computer Engineering

September 2004

Department of Electrical & Computer Engineering
Carnegie Mellon University
Pittsburgh, Pennsylvania
USA

Readers: Professor Gary K. Fedder
Professor David W. Greve

ABSTRACT

Presented in this Master's project is a microfluidic valve design, a fabrication technology, and results from test devices. The microvalve will be a component in a Direct Methanol Fuel Cell developed by Carnegie Mellon University.

The designed microfluidic valve consists of two electrostatically actuated membranes hydraulically coupled together. The substrate below the membranes has a curved profile to reduce the pull-in voltage – a phenomenon known as "zipper actuation". Three microvalves can be actuated peristaltically in series to create a pump. The membranes require no steady-state power and use no rectifying valves.

Test devices are fabricated as proof-of-concept experiments for the microvalves. The test devices have a single mesh-membrane suspended over a flat-bottomed cavity in the silicon. As a model for zipper actuation, the silicon cavities are fabricated with a "step" in the silicon to compare to completely flat cavities. Comparisons of test device performance are made with and without the hydraulic fluid in the silicon cavity.

The test devices are fabricated in a custom single-oxide layer, single metal-layer process. Stress analysis is presented for the candidate materials: thermal oxide, spin-on glass, platinum, and aluminum. Ultimately, 1 μm thermal oxide and 0.11 μm platinum are used to fabricate the devices. The mesh is released from the substrate and sealed with polymer to form the complete membrane.

The theoretical analysis of the membrane indicated that to actuate it the applied voltage is around 500 V. That voltage is impractical for this work because it is greater than the breakdown voltage of the oxide and much greater than the operational voltage of the fuel cell. At 100 V the theory indicates that the pump displaces less than 5% of its volume.

Although the fabricated beams in the mesh should lie flat when released, they still curl enough to touch the substrate. Consequently, this inhibited characterization of pull-in voltage. Future work entails improving the fabrication process to achieve working test devices and performing numerical simulations to analyze membrane behavior.

Keywords: MEMS, microfluidic, fabrication, hydraulic, pump, valve

TABLE OF CONTENTS

ACKNOWLEDGEMENTS

I would like to thank my family – my parents, Jason, Bubby, Zaddie, the Nierow family, and the Nathanson family – for instilling in me a strong sense of self and a love of learning and knowledge.

In my scientific and engineering experience, I have had great mentors over the years who've instructed me and motivated me – Denis Fermental, Joe Noonan, Karen Panetta, and Vo Van Toi at Tufts University; Mark Mescher at Draper Laboratory; Tony Charanis, Debra Gulick, and Ed Weston at East Brunswick High School; and my teachers at Solomon Schecter Day School. I have also been encouraged by the work of Richard Feynman [1] and my Uncle Alan.

Over the past two years I have been fortunate to work with some more great people in the MEMS Lab at Carnegie Mellon. First, I must thank my advisor Gary Fedder for giving me the opportunity to study at Carnegie Mellon and his valuable instruction. George Lopez Subrebost was instrumental throughout the project. John Neumann and Dan Gaugel provided lots of help in the cleanroom and in device fabrication. I also benefited from interacting with my peers — Fernando Alfaro, Sarah Bedair, Jay Brotz, Fang Chen, Peter Gilgunn, Abhishek Jajoo, and Michael Sperling. I want to thank Mary Moore for her work in holding the lab together and for editing my thesis. Phil LeDuc's instruction in mechanical analysis was also very important to my work. Thanks to the cleanroom staff: Chris Bowman, Tim Fisher, and Carsen Kline.

I also want to thank my friends in Pittsburgh for sharing in the good times and lending an ear when I needed it. Last I'd like to thank the city of Pittsburgh for proving that you really can put French fries on anything.

"Power rests on the kind of knowledge one holds. What is the sense of knowing things that are useless?"

–Don Juan [2]

1. INTRODUCTION

This paper discusses the research and development of an electrostatically actuated membrane implemented as a microvalve and the implementation of three microvalves as a micropump. These devices have a range of uses in areas from biomedical applications to portable power. This work seeks to contribute to portable power by outlining steps towards a microfluidic pump for a fuel cell and conducting proof-of-concept experiments.

1.1. Project Motivation

Fuel cells are quickly becoming an attractive alternative to conventional lithium ion batteries. For the same volume, a fuel cell has more energy and less weight than a battery. Despite these advantages, development and cost remain prohibitive factors.

Because of the opportunities presented by fuel cells, Carnegie Mellon University is developing a Direct Methanol Fuel Cell (DMFC) [5]. The advantage of the Carnegie Mellon fuel cell is:

> "compared to state-of-the-art lithium-ion batteries, the proposed DMFC will (i) provide a four-fold operating life span, (ii) exhibit a five-fold advantage on a weight basis, and (iii) lessen the environmental impact of battery disposal." [5]

In the Carnegie Mellon DMFC the concentration of the methanol solution on the anode side of the proton exchange membrane must be around 2% for maximum electro-chemical efficiency. However, the methanol reserves of the fuel cell will be most efficient if the stored methanol is 100% pure and then diluted to create the 2% methanol solution.

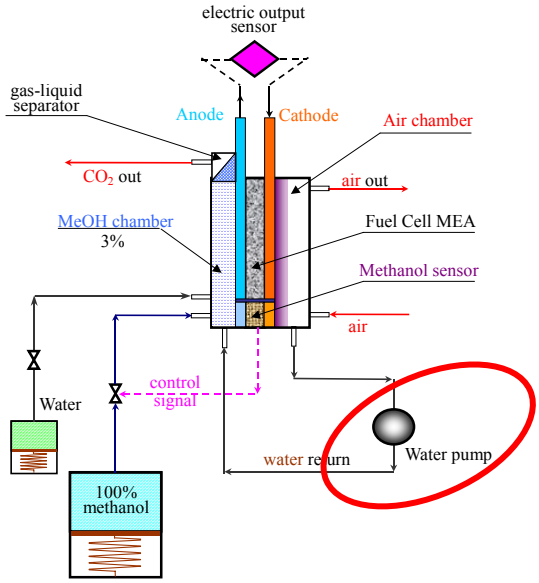

Figure 1.1. Schematic of the Direct Methanol Fuel Cell. The discussed microfluidic pump is the 'Water pump' [5].

Since part of the methanol reaction yields water on the cathode side, that water can then be pumped back to the anode to keep the 2% methanol solution diluted as shown in Figure 1.1. The proposed micropump will provide this function.

The micropump must meet certain specifications to meet the needs of the fuel cell. First, the pump will have to provide water at a pressure of 0.5 PSI (3.44 kPa) across the pump and a maximum flow rate of 0.1 cc/min (1.66 µl/sec). Next, the proposed fuel cell will produce a net output of 0.65 W which sets the limit on micropump power consumption. The micropump should operate in the range of 1 to 10 volts because that is the range of the fuel cell output voltage. Last, the pump should be of minimal size so that the maximum amount of space can be used for methanol fuel reserves.

1.2. Prior Work

Table 1.2.* A table of previous work with electrostatically actuated micropumps and microvalves.

Author and Year	Pump/ Valve	fluid type	V [V]	f [Hz]	ΔP_{max} [kPa]	Q_{max} [ml/min]
Zengerle, 1992 [7]	pump	gas	170	25	2.5	0.070
Judy, 1991 [8]	pump	gas	50-75	not reported	not reported	not reported
Cabuz, 2001 [9]	Pump	gas	165-200	35-95	1.96	30
Wagner, 1996 [10]	Valve	gas	15-50	not reported	not reported	not reported
Wijngaart [11]	Valve	gas	60-80	not reported	5-13	not reported
Recent Piezoelectric [6] (MIP Implantable)	pump	liquid	150	0.2	55	0.0017
Recent Thermopneumatic [6] (Zimmermann)	pump	liquid	not reported	10	16	0.009

There has been about two decades of work on micropumps with much focus on piezoelectric and thermopneumatic pumps [6]. Table 1.2 lists previous work with electrostatically driven micropumps and microvalves which is the focus of this report. A common theme in the gas micropumps of Cabuz, Wagner, and Wijngaart is they all use a form of zipper pull-in for electrostatic actuation.

Some of the first electrostatic pumps were done by Zengerle et al. and Judy et al. Zengerle's pumps actuated at around 170 V and were made in stacked silicon wafers with a 4.4 μm gap between electrodes [7]. Judy's surface micromachined structures also had micron-sized gaps, volume per cycle of 12 to 640 nl, and actuation voltages of 50V [8]. The Judy paper identified important device limitations: (1) The maximum voltage is determined by dielectric breakdown. (2) Surface tension limits fluid flow rates due to resulting high pressures.

Cabuz's work at Honeywell is a significant accomplishment in electrostatic micropumps [9]. The micropump can easily be placed in parallel or series to increase flow, pressure, or both.

The actuation voltage of Wagner's valve is a relatively low 15 to 50 V [10]. Wagner used grey-scale lithography to achieve the curved silicon profile for zipper

* Style and data of Table 1.2 taken from [6].

actuation. Each valve in Wagner's design consists of two pneumatically coupled membranes which give full control of both up and down motion.

Wijngaart's valve also has electrostatic zipper actuation as well [11]. One unique feature of this valve is its use of a flexible membrane with a flat substrate rather than a curved substrate. Another novel concept of this valve is that it uses the difference between inlet and outlet pressure to assist in actuation. Wijngaart describes how to determine optimal insulator thickness and actuation voltage for an electrostatic pump. Last, the paper notes a "charging phenomenon" that occurs with each consecutive actuation of the membrane causing the actuation voltage to increase over time. Wijngaart believes this comes from parasitic charging on the oxide-air interface and takes advantage of this by reversing the polarity on the electrodes after each actuation.

An analysis of electrostatic pumps using the zipper effect is provided by Saif et al. [12]. Saif specifically analyzes a single cavity and an annulus (donut) shaped cavity:

> "The study...indicates that for a given applied voltage, the pressure increases 1) almost inversely with the thickness of the dielectric between the diaphragm and the cavity floor, 2) slightly with the increase in the diaphragm thickness and elastic modulus, and 3) as the initial volume of the cavity is higher than that in the annular cavity for similar applied voltages and overall cavity sizes." [12]

Saif cites the main limitation to pump pressure as the maximum applied voltage determined by the breakdown field of the insulator, which confirms Judy's findings. Saif confirms that stress within the membrane should not cause failure since analyzed stresses are much lower than yield stresses of many glassy polymers. Last, Saif says that the membrane should be treated as a membrane and not a plate since its deflection is greater than membrane thickness. This is an important consideration in the analysis, indicating that stretching rather than bending dominates the behavior of the membrane.

A final paper worth mentioning will be useful in future membrane design. In this first generation of micropump, the membrane has uniform thickness. Kotera's paper discusses membranes of varying thickness [13]. In future micropump versions varying the membrane thickness for optimum performance would be applicable, especially if the pump is designed with multiple metal layers directly in Complimentary Metal-Oxide-Silicon (CMOS).

This research has many practical applications. Micropumps for implantable drug delivery offer new possibilities for diabetics in need of insulin and other medical conditions that require regularly delivered small amounts of drugs [3, 4]. In terms of power delivery, micropumps hold much promise in fuel cell technology. Industry has taken notice of fuel cells and companies are developing their own fuel cells [14]. Medis Technologies has developed a fuel cell "Power Pack" to power cell phones, digital cameras and similar electronic devices [15]. The Medis design is novel with regard to its proprietary sodium borohydride-based fuel and has no water management system. A competitor, MTI Micro is developing a fuel cell based on 100% pure methanol. Similar to the Medis design, MTI Micro also lacks a water management pump [16].

1.3. Project Overview

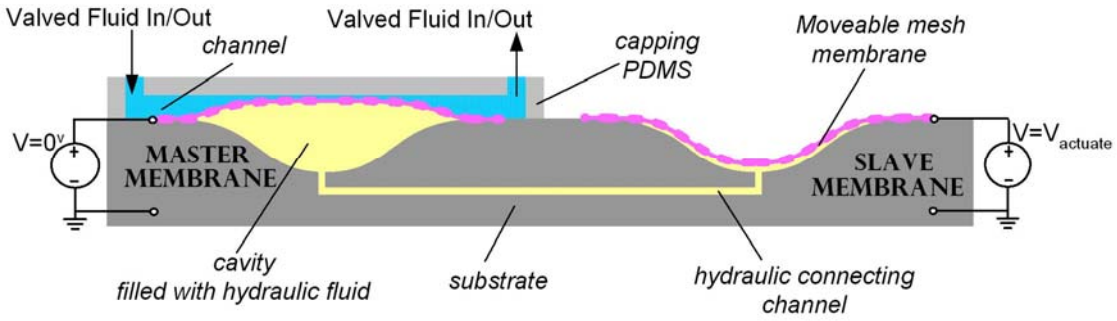

Figure 1.3. Envisioned concept: Cross section of the hydraulic microfluidic pump consisting of two membranes hydraulically coupled.

Presented in this project is a detailed conceptual analysis of the membrane as it deflects under pressure, conceptual valve fabrication, and experimental tests. Shown in Figure 1.3, the proposed valve consists of two electrostatically actuated membranes above cavities filled with a dielectric fluid that hydraulically couples the membranes together. There are two separate fluids in the valve: "Hydraulic fluid", located between the membranes and the substrate, which couples the two membranes together and "valved fluid" which flows in and out of the void formed above the master membrane. Electrostatically actuating the "master" membrane expels its hydraulic fluid which forces the "slave" membrane to rise. To return the pump to its original state, the slave membrane is actuated by applying a voltage between the membrane and substrate. The ultimate purpose of the valve is to control the valved fluid.

The proposed valve will be driven by electrostatic forces which offer advantages over other types of actuation, such as thermal and piezoelectric, in that it is lower power and lower voltage, respectively. Further reducing power consumption, electrostatic actuation uses power only when changing states, not in steady state conditions.

1.4. Valve Concept

The master valve shown in Figure 1.3 consists of a membrane suspended above a cavity in a silicon substrate filled with insulating hydraulic fluid. The membrane deflects by applying a voltage between the metal embedded within the membrane and the silicon. The electrostatic force from the applied voltage is balanced by the restoring tensile force of the membranes and the pressure in the hydraulic fluid. "Pull-in" occurs when the voltage reaches a critical value, $V_{pull\text{-}in}$, the master membrane snaps down to the substrate because the membrane's mechanical restoring force and the pressure in the fluid can no longer balance the electrostatic force. When the master membrane moves down toward the substrate, the "valved" fluid is sucked into the gap created in the cavity formed above it. At the same time the master membrane expels the hydraulic fluid into the cavity of the slave membrane. Finally, actuating the slave membrane forces the hydraulic fluid into the master cavity and returns the master membrane to its original position. The idea of coupled membranes is based on Wagner, et al. [10]. As the membrane returns to its original position, it closes the channel above the master membrane which expels the valved fluid from the channel.

In this design there are many trade-offs – some which limit the device's functionality and others that are used for an advantage. The trade-off between the applied voltage and the restoring force of the membrane is taken advantage of. The stiffer the membrane, the larger the restoring force for a given deflection. As the restoring force gets larger, a larger voltage will be needed to deflect the membrane. Balance must be found between a membrane that is so stiff it needs a very high $V_{pull\text{-}in}$ versus a very floppy membrane that is too weak to push out the valved fluid above it. By having the hydraulic fluid provide most of the restoring force for the membrane, this trade-off is eliminated by allowing the membrane to be as floppy as possible. Further, using the hydraulic fluid allows active control of membrane motion, whereas relying on the restoring force of the membrane passively controls upward motion.

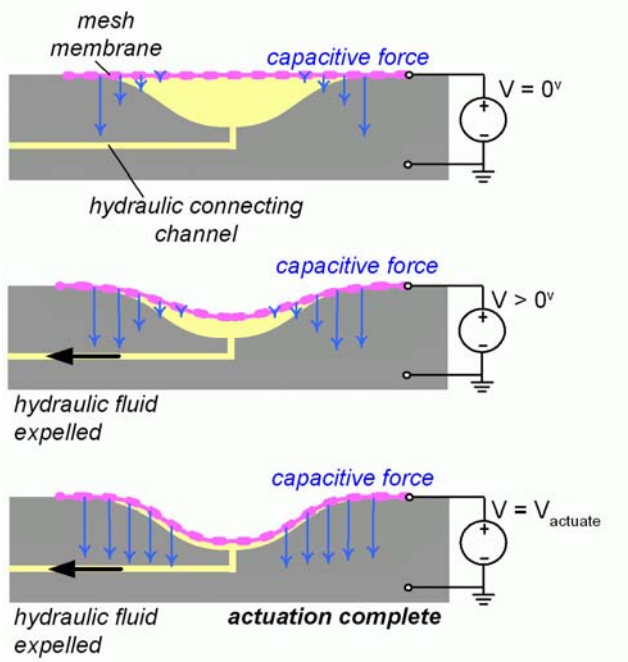

Figure 1.4. Diagram of the "zipper effect": The force is stronger where the gap is smaller. When the membrane pulls down at the edges the forces increase on the rest of the membrane, further pulling it down.

Another trade-off is between cavity depth and $V_{pull\text{-}in}$. Suspended above the silicon, the membrane acts as a movable electrode. As with any capacitor, the force grows larger when the gap gets smaller. By making the depth of the cavity very small, hence a small gap between the electrodes, a small $V_{pull\text{-}in}$ will actuate the membrane. However, the cavity depth also determines the volume of the valved fluid. Since the valves are ultimately components of a pump, the pump's stroke volume depends on the depth of the cavity. To tackle this trade-off, the valve has a curved substrate giving it both a large stroke volume and a low pull-in voltage which is referred to as the "zipper effect".

The key to the zipper effect is that it takes advantage of capacitive force by having the pull-in propagate along the radius of the membrane [12, 9]. Electrostatic force varies as 1/distance^2. That means as the distance between the membrane and substrate becomes small, the electrostatic force greatly increases. Since the gap between the membrane and substrate is smallest at the edges as shown in Figure 1.4, there is a large force which pulls in the membrane at the edges. That pull-in deflection pulls the whole membrane a bit closer to the substrate. This propagates along the membrane causing it to 'zipper' down all the way.

1.5. Pump Concept

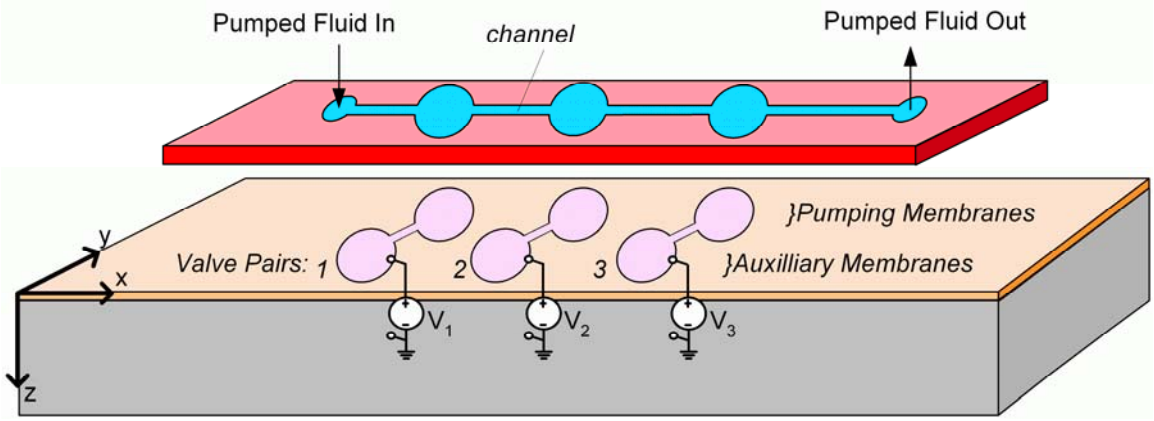

Figure 1.5. Diagram of microfluidic pump of peristaltically actuated microvalves.

Although the valve is the focus of this work, the ultimate goal is a micropump. Three valves can be used in series to form a peristaltic pump as in Figure 1.5. Since the master and slave convention dictates that two membranes are needed to fully control one valve, each "pumping" membrane for the pumped fluid requires its own "auxiliary" membrane. In this setup, actuating the valves moves the pumped fluid through the channel. Since the order of pump actuation determines the direction of fluid flow, the pump can move fluid in either direction. The peristaltic motion requires no rectifying valves. To move the pumped fluid the valves should be actuated in the following sequence:

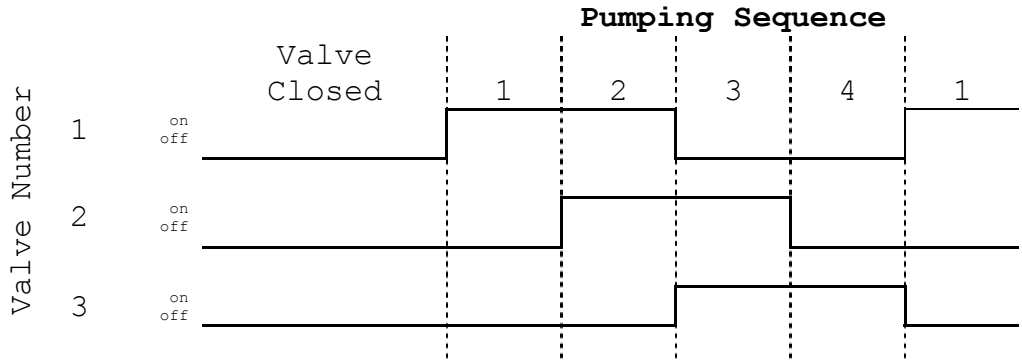

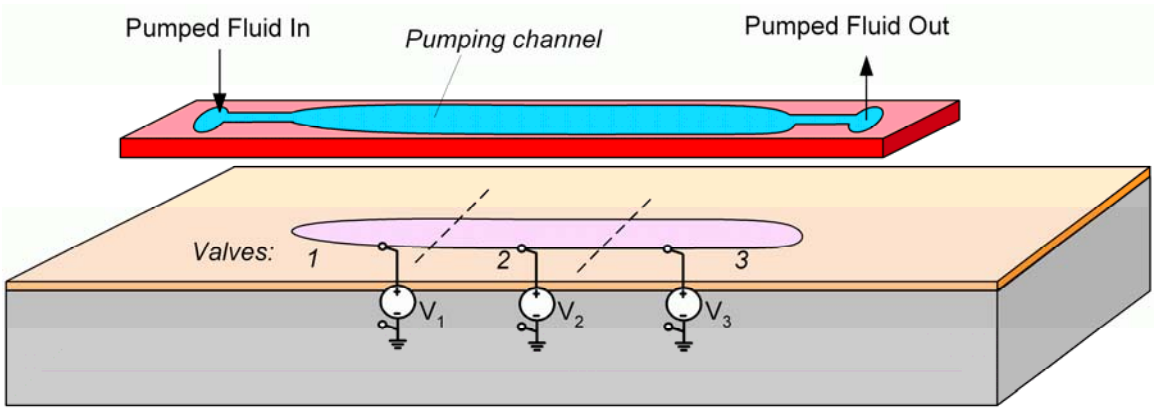

Figure 1.6. Advanced "bathtub" design of the micropump.

While this pump design is certainly suitable, a more advanced design is proposed as well. In the advanced design the channel is eliminated between each individual valve. Further, rather than having pumping valves hydraulically coupled to auxiliary valves, the three pumping valves are hydraulically coupled to each other. In the advanced design shown in Figure 1.6 the membrane is physically continuous, but electrically divided into three separate pumping areas.

1.6. Scope

The ultimate goal of this work is to create a working micropump that is integrated in the Direct Methanol Fuel Cell. To achieve that, this Master's project report will determine a preliminary fabrication technology in which to create the micropump. Further, basic test structures will be fabricated to prove the proposed concepts. To prove the zipper actuation, a flat-bottomed cavity will be compared to a simplified version of a curved cavity. The test structures will consist of three designs of a membrane suspended over: (1) a shallow flat silicon cavity, (2) a deeper flat silicon cavity, and (3) a two-tiered silicon cavity – as a simplified version of the curved cavity design. A second proof-of-concept test will be to fill the cavities with a dielectric fluid and examine the effect on performance. Further work with the membranes – such as creating a working valve or linking them together to form a pump – is beyond the scope of this project. Thus, this Master's project report will lay the groundwork for device fabrication, design, and testing.

2. THEORY

2.1. Analysis Overview

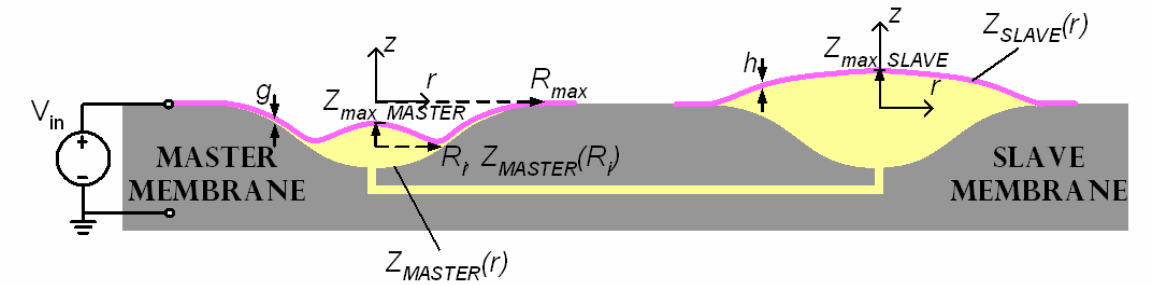

Figure 2.1. Cross-section diagram of variables as they relate to the valve.
Note: The master membrane is drawn with a thin layer of hydraulic fluid between it and the substrate to indicate that the membrane is not attached to the substrate except at the edges where there is no hydraulic fluid.

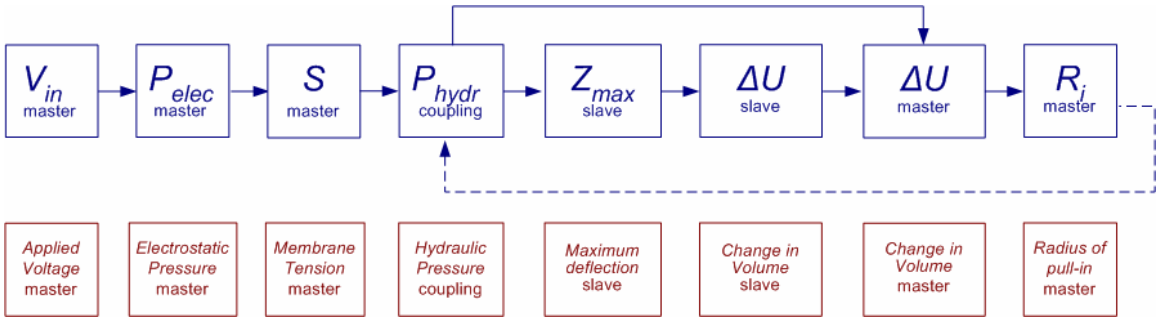

Figure 2.2. Diagram of equations related to membrane position of the microvalve. The solid lines indicate the variables used to solve an equation. The dashed lines indicate where a value from the previous iteration is used.

The microfluidic valve system is shown in cross-section in Figure 2.1; from the top view, the membranes are circular. The behavior of the valve is controlled by interrelated equations of electrical, hydraulic, and mechanical forces, as diagramed in Figure 2.2. An applied voltage, V_{in}, causes the master membrane to pull-in to a radial distance, R_i, displacing a volume ΔU_{MASTER}. An electrostatic pressure, P_{elec}, generated by V_{in} , and causes the master membrane to pull down to the substrate, displacing some of its hydraulic fluid. Since the hydraulic fluid is incompressible, its pressure, P_{hydr}, increases from the applied pressure of the master membrane and slave. S_{MASTER} is the tension per unit length, in units of N/m, caused by the stretching of the master membrane. Because the valve is in static equilibrium, S_{MASTER} is proportional to P_{elec}. S_{MASTER} and R_i determine the value of P_{hydr}. Since both membranes are equally subjected to the hydraulic pressure, S_{SLAVE} must balance P_{hydr} as well. The stress in the slave membrane causes strain that is the difference between the original length, $2R_{max}$, and the length of

the new shape, $Z_{SLAVE}(r)$, which in turn determines its change in volume, ΔU_{SLAVE}. Because the cavities are connected, any increase in ΔU_{SLAVE} is offset by a decrease in ΔU_{MASTER}. Finishing the set of equations, ΔU_{MASTER} is a function of R_i and P_{hydr}.

To iterate on the set of equations and converge to a solution, the value of R_i from the i^{th} iteration is used to calculate $P_{hydr,i+1}$ in the $i+1^{th}$ iteration. Eventually the values of R_n and R_{n-1} converge to the final R value. To start out, the value of $R_{i=0}$ is set to $R_{max}/2$ in the first iteration.

2.2. Detailed Analysis

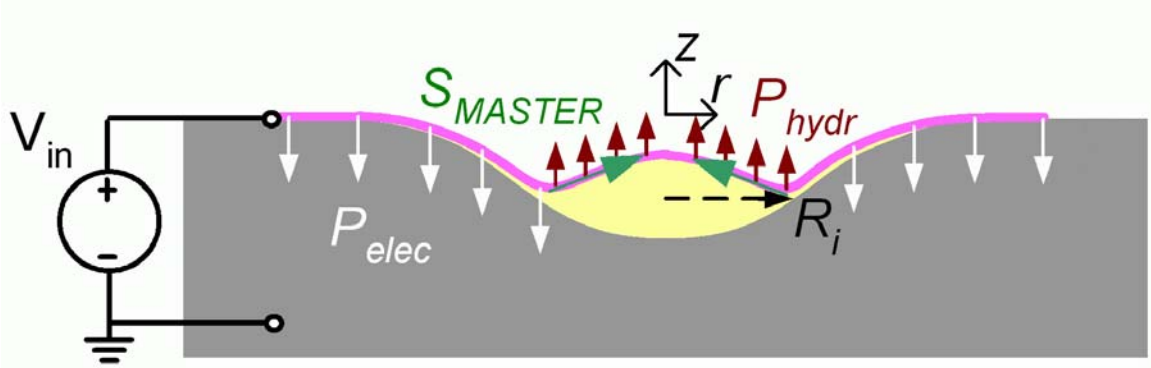

Figure 2.3. Cross-section diagram of variables as they relate to the valve.

The driving force of the valve is an electrostatic force due to an applied voltage between the membrane and the substrate. For the geometry used in fabrication, 59.25% of the membrane area contributes to the electrostatic force. Hence the electrostatic pressure is:

$$P_{elec} = \frac{F_{cap}}{A} = 0.5925 \frac{V_{in}^2}{2} \frac{\varepsilon_0 \varepsilon_r}{g^2} \tag{2.1}$$

where ε_0 is the permittivity of vacuum, relative permittivity is ε_r, and the gap between electrodes is g.

P_{elec} varies with the gap, having two distinct regions: contact, $r = R_i$ to 0, and non-contact, $r = R_i$ to R_{max}. According to Saif, the capacitive force of the contact region is much greater than the non-contact region, hence the non-contact region $R < R_i$. can be ignored (Figure 2.3) [12].

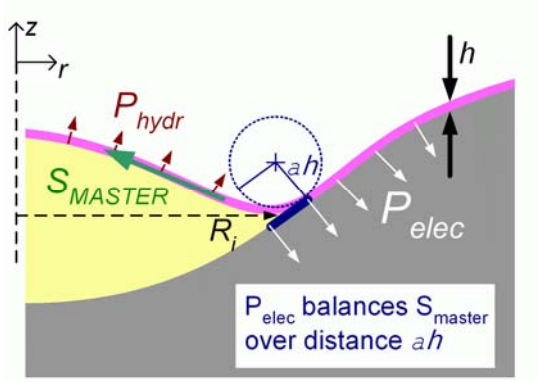

Figure 2.4. Detail of the cross-section detailing the forces at R_i. Even though the membrane starts to peel off at R_i, it's approximated as a region in contact over αh.

The membrane bending at the contact point R_i is modeled as circular with a radius of αh where h is the membrane thickness and α is a chosen constant relating membrane thickness to the length of the membrane that contributes to electrostatic pressure (Figure 2.4).

In this analysis, it is assumed that: A) there is no hydraulic fluid between the membrane and substrate in the contact region; B) S_{MASTER} at the contact point, R_i, is balanced by P_{elec} over the short annulus of width of αh; C) P_{hydr} is not in the equation $S_{MASTER} = f(P_{elec})$ because it acts orthogonally to those forces; D) P_{elec} in the contact region annulus of width of $r = R_i$ to R_{max} does not affect membrane tension. Under those assumptions, the tension per unit length is:

$$S_{MASTER} = (P_e)(\alpha h) \tag{2.2}$$

Since S_{MASTER} must balance the hydraulic pressure in the non contact region $r = 0$ to R_i. the hydraulic pressure is [12],

$$P_{hydr} = \sqrt{\frac{E}{1-\nu^2}\frac{h}{24}S_{MASTER}^3 R_i^2} \tag{2.3}$$

where E is Young's Modulus, ν is Poisson's ratio.

According to analysis by Timoshenko plates under uniform pressure, such as the slave membrane, have three different analysis types: plates under small deflection, plates under large deflection, and membranes which are respectively driven by forces of bending only, bending and stretching, and stretching only [17]. The ratio between deflection and plate thickness determines the type of analysis. Small deflections (less than half the plate thickness) are dominated by bending and very large deflections (many times the plate thickness) are dominated by stretching. It is important to make a valid

assumption regarding the analysis type because each type is valid only under certain conditions. This work assumes deflection many times the plate thickness and, consequently, membrane analysis.

Interestingly, the equation governing shape is always the same for both deflected plates and membranes under uniform pressure [17]:

$$Z_{SLAVE}(r) = Z_{\max}\left(1 - \frac{r^2}{R_{\max}^2}\right)^2 \tag{2.4}$$

The maximum displacement, Z_{max}, is the parameter in Equation 2.4 that differs based on the type of analysis. Given P_{hydr}, the maximum deflection of the slave membrane is:

$$Z_{\max\_SLAVE} = 0.662 R_{\max}\left(\frac{P_{hydr} R_{\max}}{Eh}\right)^{1/3} \tag{2.5}$$

The integral of the shape yields the displaced volume under the slave membrane

$$\Delta U_{SLAVE} = \int_0^{R_{\max}} 2\pi r Z_{SLAVE}(r)\,dr \tag{2.6}$$

Solving the integral for U_{slave} shows:

$$\Delta U_{SLAVE} = \frac{\pi}{3} R_{\max}^2 Z_{\max\_SLAVE} \tag{2.7}$$

The cavity below the slave membrane is connected to the cavity below the master membrane. Thus any increase in volume from the slave cavity must be due to a decrease in volume from the master cavity.

$$\Delta U_{MASTER} = -\Delta U_{SLAVE} \tag{2.8}$$

The final step in the iteration is to find R_i for ΔU_{MASTER}. In the non-contact region, the membrane stretches under the pressure P_{hydr}. Similar to the slave membrane, this stretching is governed by Z_{max_MASTER}, the maximum height of the master membrane under uniform pressure above the anchor points $Z_{MASTER}(R_i)$.

$$Z_{\max\_MASTER} = 0.662 R_i\left(\frac{P_{hydr} R_i}{Eh}\right)^{1/3} - Z_{MASTER}(R_i) \tag{2.9}$$

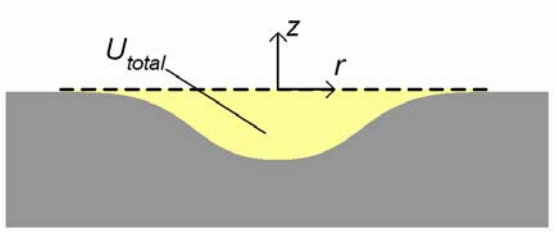

The total volume under the master membrane at rest, U_{total},

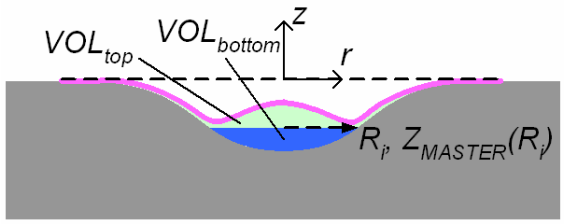

minus the volume under the non-contact region of the actuated master membrane, $U_{top} + U_{bottom}$,

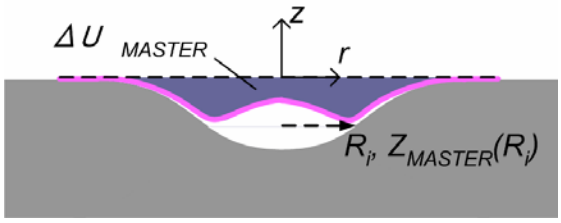

equals the displaced volume, ΔU_{MASTER}.

Figure 2.5. Cross-section diagrams of the valve illustrating the calculation of ΔU_{MASTER} by subtracting the volume below the non-contact region from the total volume.

The calculation of ΔU_{MASTER} is shown schematically in Figure 2.5. The displaced volume equals the volume under the non-contact region subtracted from the total membrane volume, assuming no hydraulic fluid in the contact region. The total volume of hydraulic fluid under the membrane in the undeflected state is:

$$U_{total} = \frac{-1}{2} \frac{Z_{\min} R_{\max}^2 \left(\pi^2 - 4\right)}{\pi} \tag{2.10}$$

The portion of fluid labeled in Figure 2.5 as U_{top} is:

$$U_{top} = \frac{\pi}{3} k^2 R_{\max}^2 Z_{\max\_MASTER} \tag{2.11}$$

U_{bottom} in Figure 2.5 is:

$$U_{bottom} = \frac{-1}{2\pi} Z_{\min} R_{\max}^2 \left(\pi^2 k^2 + 2\cos(k\pi) + 2\pi k \sin(k\pi) - 2\right) \tag{2.12}$$

The equations are simplified by defining k as:

$$k = \frac{R_i}{R_{\max}} \tag{2.13}$$

And the substrate has a cosine shape given by:

$$Z_{MASTER} = \frac{-Z_{\min}}{2} \left(1 + \cos\left(\frac{r\pi}{R_{\max}}\right)\right) \tag{2.14}$$

Thus the displaced volume, ΔU_{MASTER}, is:

$$\Delta U_{MASTER} = U_{total} - U_{top} - U_{bottom} \tag{2.15}$$

The equation for $R_i = f(\Delta U_{MASTER})$ cannot be determined explicitly; therefore, Newton's method is used to determine the value of R_i corresponding to ΔU_{MASTER}.

The data input in the equations was based on the fabricated test devices. Since these membranes are in the Simsox process where the Young's modulus of the membrane is unknown, that value is taken from Zeleznik's analysis of a similar polymer-coated-mesh membrane which had a Young's modulus of about 1 GPa [18]. The coupling fluid in the experiments was Gelest DMS-T05 silicone oil which has a viscosity of 5.0 cSt, or 4.59 cP, and dielectric constant of 2.60. The metal mesh is 0.1 µm thick and sealed with 1.5 µm of polymer on both sides for a total membrane thickness of 3.1 µm. The maximum applicable voltage is dependant on the dielectric material. The fabricated devices have 1 µm of thermal oxide for electrical insulation, where Madou lists the maximum breakdown field as 3 MV/cm resulting in a maximum voltage of 300 V [19].

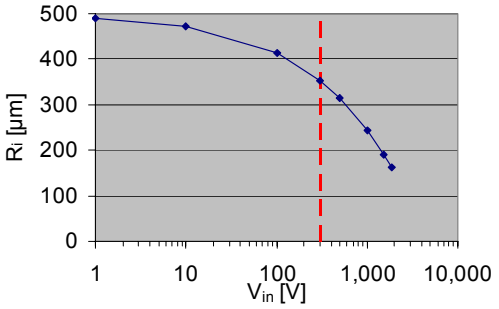

(a) R_i vs. V_{in}

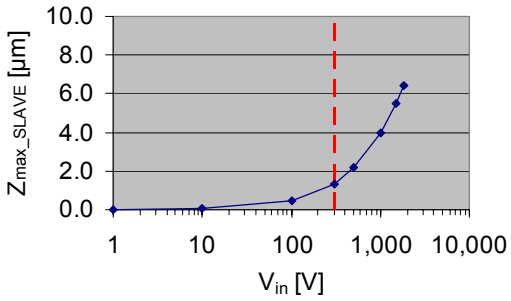

(b) Z_{max_SLAVE} vs. V_{in}

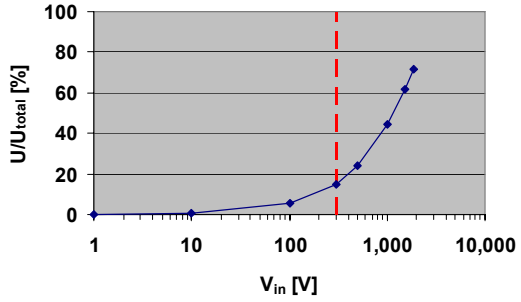

(c) Percent volume displaced vs. V_{in}

Figure 2.6. Graphs where the solid line shows the effect of V_{in} on two membranes hydraulically coupled together. The dashed line indicates the maximum applicable voltage before dielectric breakdown.

The 500 µm radius membrane is modeled in Figure 2.6 given the conditions: ε_0 = 8.85*10^{-12} F/m, ε_r = 2.6, g = 1*10^{-6} m, alpha = 10, h = 3.1*10^{-6} m, Z_{min} = 10*10^{-6} m, E = 1*10^{9} Pa, and v = 0.20. The total volume below the master membrane is -2.33*10^{-12} m^3 or -2.33 pl; for comparison, a cylinder of the same radius R_{max} and height Z_{min} has a volume of 7.85*10^{-12} m^3 or 7.85 pl.

The results shown in Figure 2.6 indicate the limitations of the device. R_i was the value sought in the equations, but two more telling variables are Z_{max_SLAVE} and percent volume displaced. When the membrane bulges up into the channel containing the valved fluid Z_{max_SLAVE} indicates how high it bulges and if it will seal the channel. At the maximum voltage, 300 V, R_i = 354 µm, Z_{max_SLAVE} = 1.3 µm, and the percent volume displaced is 15 %. The maximum output voltage of the fuel cell, where the pump will eventually be a component, is 10 V. At V_{in} = 10 V, R_i = 471 µm, Z_{max_SLAVE} = 0.05 µm, and the percent volume displaced is 1 % -- almost no change.

2.3. Test Membrane Analysis

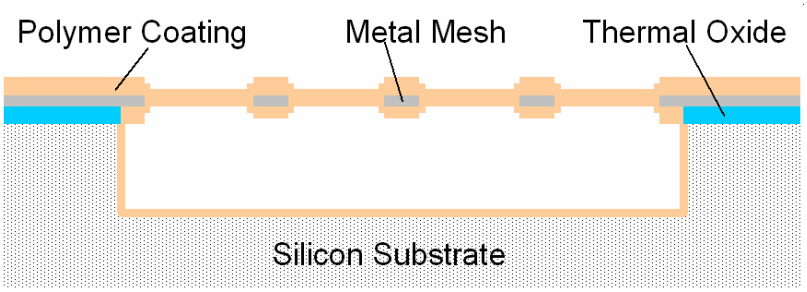

Figure 2.7. Cross-section of a test device structure.

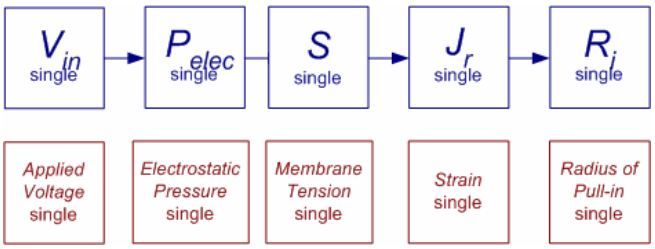

Figure 2.8. Diagram of equations related to membrane position of the test device.

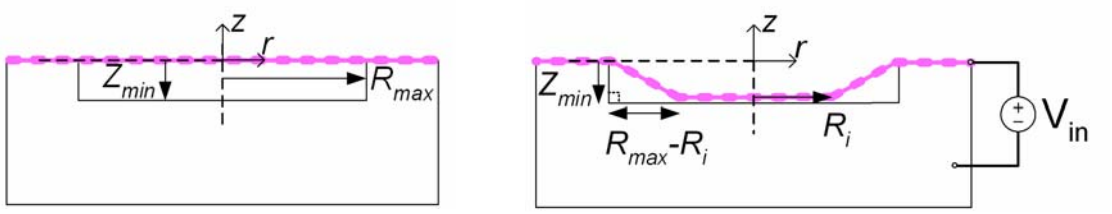

(a) Membrane at rest (b) Membrane at pull-in

Figure 2.9. Cross-section of the test membrane.

As a proof-of-concept, the test device structure in Figure 2.7 is fabricated and tested. The test device is a single membrane over a cavity. Two forces control the membrane: an electrostatic force pulls the membrane to the substrate and the mechanical restoring force of the membrane returns it to the rest position. The relationship between the governing equations is shown in Figure 2.8.

Figure 2.9 shows the theoretical model of the test device. When the voltage is large enough, $V_{pull\text{-}in}$, the membrane snaps down to the substrate. When the membrane contacts the substrate the electrostatic pressure, P_{elec}, balances the tension in the membrane S_{MASTER}. S_{MASTER} is caused by the stress of the new shape of the membrane and the resulting strain, ε_{r_strain}. Where the membrane is in contact with the substrate, there is no change in length, hence no strain. Over the region $r = R_i$ to R_{max}, the membrane stretches where the new length is $\sqrt{(R_{\max} - R_i)^2 + Z_{\min}^2}$; therefore, ε_{r_strain} determines the pull in point, R_i.

The equations relating V_{in} to P_{elec} to S_{MASTER} are the same as for the microvalve and have been explained previously. ε_{r_strain} by definition relates to S_{MASTER} as [12]:

$$\varepsilon_{r\_strain} = S_{MASTER} \frac{1-\nu^2}{Eh} \tag{2.16}$$

The strain, ε_{r_strain}, of the membrane is:

$$\varepsilon_{r\_strain} = \frac{\sqrt{(R_{\max} - R_i)^2 + Z_{\min}^2} - (R_{\max} - R_i)}{(R_{\max} - R_i)} \tag{2.17}$$

Solving for R_i:

$$R_i = R_{\max} - \frac{Z_{\min}}{\sqrt{\varepsilon_{r\_strain}^2 + 2\varepsilon_{r\_strain}}} \tag{2.18}$$

This analysis will yield $R_i = f(V_{in})$ after pull-in. As V_{in} increases, the contact area of the test membrane will increase along increasing R_i. Note that the direction of propagation of the contact area for the test device is outwardly radial, which is opposite

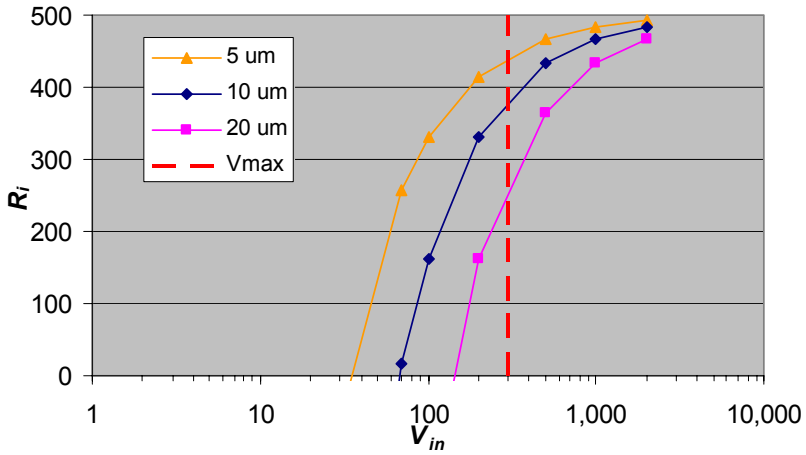

Figure 2.10. Graph where the solid line shows the effect of V_{in} on the test device for different values of pit depth, Z_{min}. The dashed line indicates the maximum applicable voltage before dielectric breakdown.

that of the microvalve. Increasing V_{in} increases ε_{r_strain} causing R_i to approach its limit, R_{max}. Decreasing V_{in} will eventually reduce the electrostatic pressure such that it cannot balance the strain causing the membrane to release from the substrate and return to the rest position. The equations are plotted in Figure 2.10 using the same values as in Figure 2.6, except the pit depth, Z_{min}, varied as indicated. Just as in the microvalve, dielectric breakdown determines V_{max}.

The graph in Figure 2.10 shows that, as expected, R_i approaches R_{max} = 500 µm as V_{in} gets large. Also consistent with the expectations is that V_{in} must be greater than a minimal value before the electrostatic force is greater than the tension in the membrane. For example, in the case of Z_{min} = 5 µm, the minimal voltage is 34 V.

2.4. Fluid Damping

When the membrane is actuated it snaps down to the substrate. As the membrane moves it displaces the fluid below it – air in an unfilled cavity or hydraulic oil in a filled cavity. The velocity at which the membrane moves is governed by the equation for squeeze film damping between two plates [20]:

$$F_B = \frac{\mu W L^3}{g^3}\frac{dz}{dt} \tag{2.19}$$

Where F_B is the damping force applied to the membrane, μ is the dynamic viscosity, W is the width, L is the length, g is the gap between the membrane and the substrate, and dz/dt is the membrane velocity in the z-direction. Thus there is an inversely proportional relationship between dynamic viscosity and speed:

$$\frac{dz}{dt} = C_{const}\frac{1}{\mu} \tag{2.20}$$

Which in this case, means that the effect of viscosity on damping is the same for both silicone oil and air regardless of the geometry and applied voltage. The hydraulic fluid used to test the devices is trimethylsiloxy terminated polydimethylsiloxane (PDMS) purchased from Gelest, Inc. with a listed kinematic viscosity of 5 cSt and a calculated dynamic viscosity of 4.59 cP [101,21,22]. So, the relative speed of the membrane in air is:

$$\frac{dz}{dt} = C_{const}\frac{1}{\mu_{air}} = C_{const}\frac{1}{0.0182cP} = C_{const}55\,{}^{1}\!\!\diagup\!\!{}_{cP} \tag{2.21}$$

The dynamic viscosity of air is 0.182 cP [23]. Hence the relative speed of the membrane in silicone oil is:

$$\frac{dz}{dt} = C_{const}\frac{1}{\mu_{silicone}} = C_{const}\frac{1}{4.59cP} = C_{const}0.2\,{}^{1}\!\!\diagup\!\!{}_{cP} \tag{2.22}$$

So *dz/dt* is about 250 times faster in air than silicone oil.

3. DESIGN AND FABRICATION

3.1. Device Design

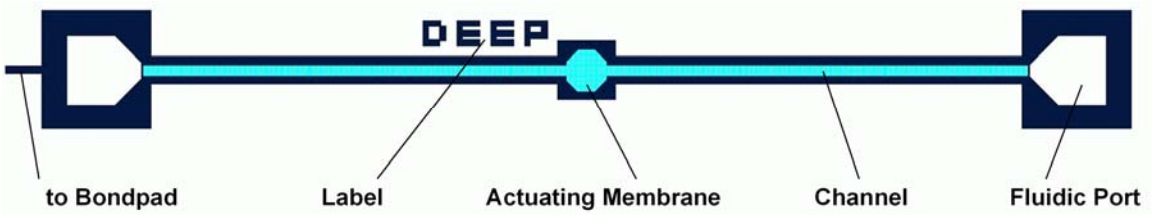

Figure 3.1. Top view of test device with a 500 µm diameter membrane and 5 mm long channels. The label indicates if the silicon below the mesh is DEEP, MIXED, or SHALLOW.

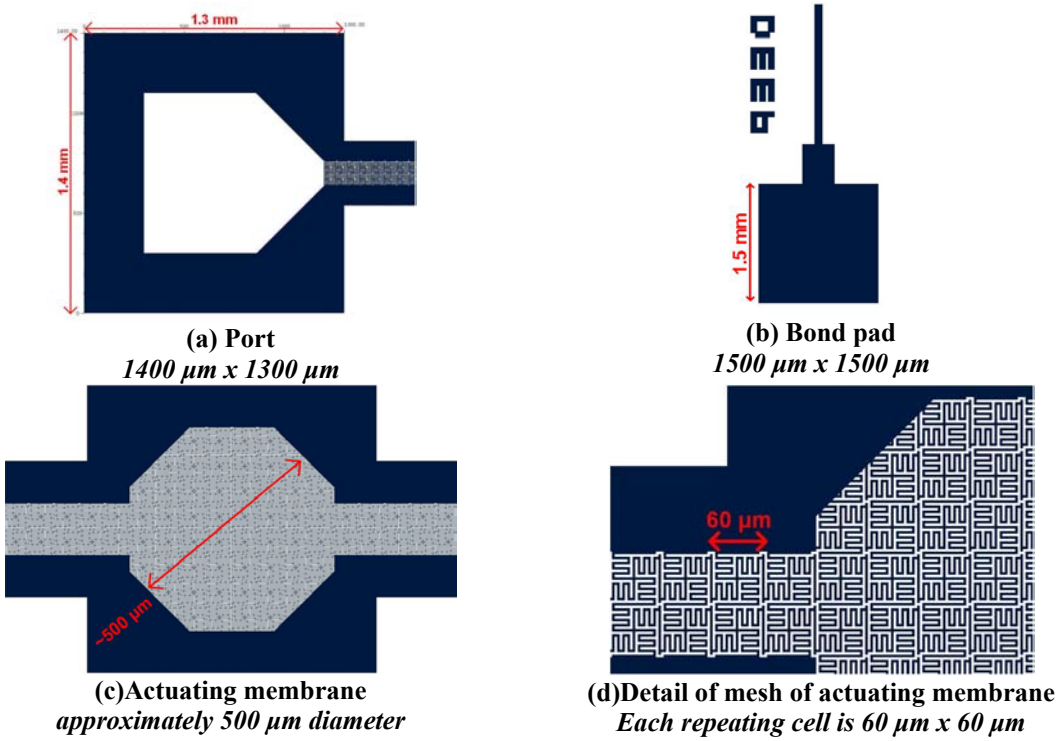

(a) Port
1400 µm x 1300 µm

(b) Bond pad
1500 µm x 1500 µm

(c)Actuating membrane
approximately 500 µm diameter

(d)Detail of mesh of actuating membrane
Each repeating cell is 60 µm x 60 µm

Figure 3.2. Detailed top view of different parts of the 500 µm diameter test device.

The ultimate goal of this work is to create a valve as in Figure 1.3. To achieve that, test devices are used to show proof of concept. The test devices have a metal mesh suspended over a silicon cavity, anchored at the edges to thermal oxide on top of the silicon as in Figure 3.1. The design of the test device consists of three main parts: actuating membrane, connections, and input/output (I/O). Figure 3.1 shows the top layer layout of a 500 µm diameter test device and Figure 3.2 details different parts of the test device.

The fluidic ports allow the hydraulic fluid to enter the cavity below the membrane. By connecting the ports to the actuating membrane with a 5 mm channel, the

fragile membrane is more easily protected from harm during application of the hydraulic fluid. Similarly, the bond pads are located far from the actuating membrane to reduce the chances of damage during probing.

The silicon under the membrane is shaped with a two-tier height profile to model the curved substrate design. The goal of the test devices is (1) to prove that the mesh and membrane really do actuate and (2) to see the effect of the curved substrate on $V_{pull\text{-}in}$. The test devices are filled with hydraulic fluid, but the fluid will not couple membranes.

3.2. Fabrication Challenges

To achieve the desired functionality of the valve and test devices, the fabrication technology must meet certain criteria. The membrane must have a conductive layer to apply the voltage to and a dielectric layer to prevent a short circuit to the substrate. Also, the membrane must be liquid-tight so that the hydraulic fluid is completely separated from the valved fluid. Below the membrane, the substrate will have a varying profile. Finally, the valve must have both an electrical and a fluidic input/output interface. A process was developed consisting of a single oxide layer with a metal layer dubbed the Simsox process from SIngle Metal Single OXide. The Simsox process is an economical means of fabricating test devices for the microvalve on a complete wafer.

One of the major challenges in any microfluidic system is coupling the fluidics off-chip. The key is to get macro-sized tubes onto a micro-sized chip. For initial testing it is easiest to put the device on a wafer with large inlet and outlet holes far from the working device. For that reason, the first pumps and test devices are fabricated on a whole wafer rather than on individual chips.

Another issue of concern is severe beam curvature which has been seen in previous work with single-metal single-oxide beams in the lab within the Carnegie Mellon course “18-414: Introduction to MEMS”. Careful matching of material residual stress is needed to achieve flat, usable structures. Therefore, the approach to fabrication is to precisely characterize each material to properly balance their intrinsic stresses to provide adequately flat microstructures.

3.3. Simsox Process

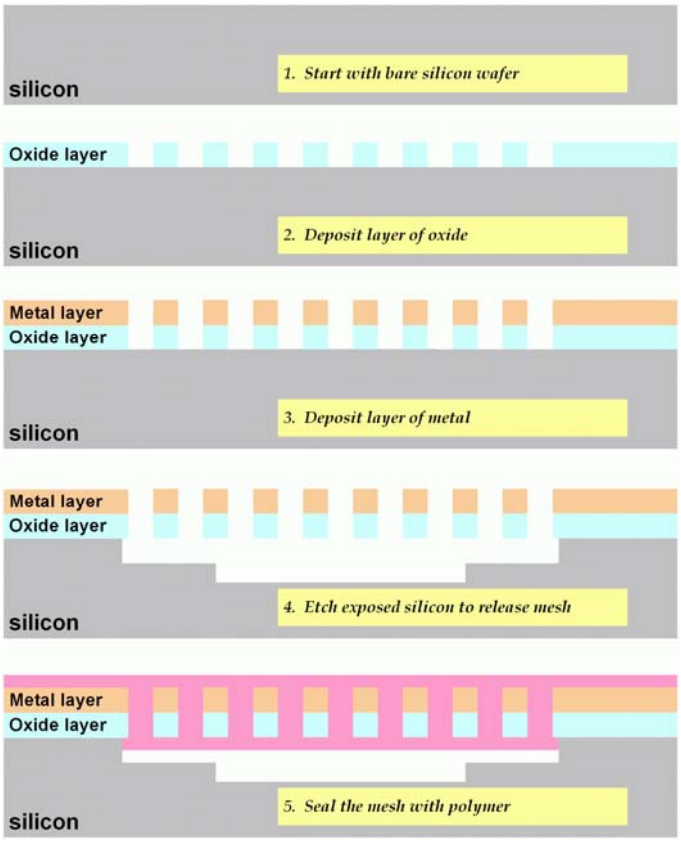

Figure 3.3. Overview of the Simsox process

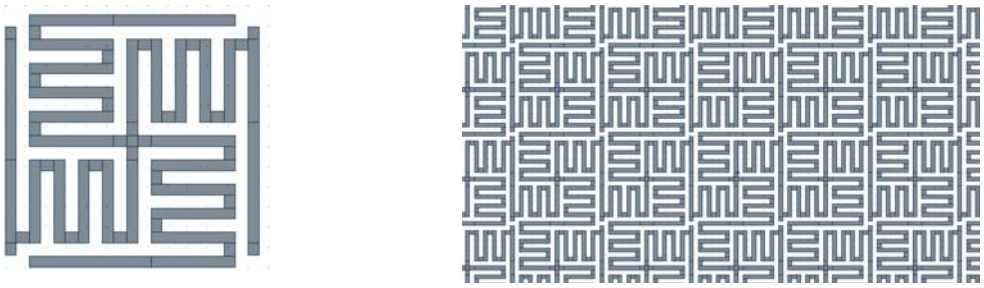

(a) (b)

Figure 3.4. The single cell in (a) is arrayed to form the mesh in (b).

To create the membrane, a mesh is etched out of the metal and oxide. The gaps in the mesh expose the silicon during an undercut etch. Finally the released mesh is coated with polymer to form a membrane. An overview of the generic Simsox process flow is shown in Figure 3.3 and Appendix D details the specific process flow.

The mesh shown in Figure 3.4 was originally developed by Neumann and consists of a single cell repeated in an array [24]. The single cell is made up of a serpentine

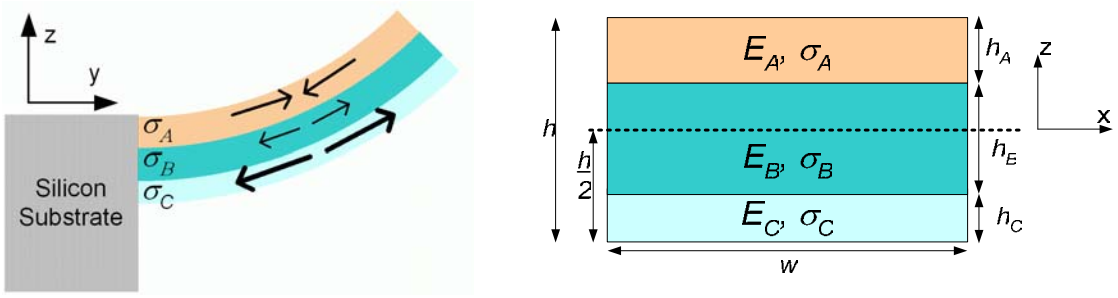

(a) (b)

Figure 3.5. (a) Side view of a beam of three materials, A, B, and C, which bends due to a moment from the different material stresses indicated by the arrows. (b) Cross section of the beam structure detailing material properties and dimensions.

pattern of beams repeated four times within the cell. Within the cell, the variables are the width of the beams, the spacing between the beams, and the number of turns made by the beams. These factors, determine the cell length and width. The resolution of the DWL66 Heidelberg Direct Write Laser lithography system used to make the mask determined the minimum feature size of the mesh. In this project, the beam width is 3 µm, the spacing is 3 µm, and there are 3 turns resulting in a total cell area of 60 µm x 60 µm. The total metal area of the cell is 2133 μm^2 or 59.25%. Cell height is governed by the thickness of the materials of the beams. These cell variables along with the properties of the polymer determine the behavior of the membrane.

The fundamental criterion for the process is that the curl in the released mesh had to be small enough for the polymer to seal it to form the membrane. For material characterization, each material is deposited on a bare silicon wafer. Film stress is determined by material thickness, h, wafer curvature before material deposition, $1/\rho_{without\_film}$, and after material deposition, $1/\rho_{with\_film}$. These properties are then analyzed to determine which combinations of film thickness and stress would produce suitably flat structures.

In developing the Simsox process, different materials were considered and analyzed. Thermal oxide and spin-on glass (SOG) were considered as candidate insulating materials. Aluminum and platinum were considered as possible conducting materials. Initial tests showed that aluminum is tensile, SOG is tensile and thermal oxide is compressive. A combination of all three materials, as in Figure 3.5, is considered to get a beam that would have a balanced stress gradient and minimal curvature.

3.4. Film Stress

Figure 3.5 shows that the stress gradient in the beams of the mesh causes it to bend with a certain radius of curvature, ρ, when released from the silicon substrate. The curvature, $1/\rho$, of the released beams is determined by the thickness and stress of the materials:

$$\frac{1}{\rho} = \frac{M}{(EI)_{effective}} \tag{5.1}$$

where M is the moment, E is Young's modulus, I is moment of inertia, and $(EI)_{effective}$ is the effective stiffness of the composite beam. $1/\rho$ is calculated for a composite beam of three layers by calculating M and $(EI)_{effective}$:

$$\frac{M}{w} = \frac{\sigma_C}{2}\left(\left(-\frac{h}{2}+h_C\right)^2 - \frac{h^2}{4}\right) + \frac{\sigma_B}{2}\left(\left(\frac{h}{2}-h_A\right)^2 - \left(\frac{-h}{2}-h_C\right)^2\right) + \frac{\sigma_A}{2}\left(\frac{h^2}{4} - \left(\frac{h}{2}-h_A\right)^2\right) \tag{5.2}$$

$$\frac{(EI)_{effective}}{w} = \frac{E_C}{3}\left(\left(\frac{-h}{2}+h_C\right)^3 + \frac{h^3}{8}\right) + \frac{E_B}{3}\left(\left(\frac{h}{2}-h_A\right)^3 - \left(\frac{-h}{2}+h_C\right)^3\right) + \frac{E_A}{3}\left(\frac{h^3}{8} - \left(\frac{-h}{2}+h_A\right)^3\right) \tag{5.3}$$

where h is the total beam height, $h_{<A,B,C>}$ is the height of each material, $E_{<A,B,C>}$ is the Young's modulus of each material, $\sigma_{<A,B,C>}$ is the stress of each material, and w the width of the beam shown in Figure 3.5.

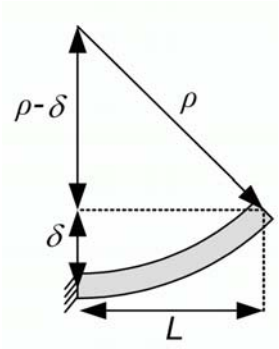

Figure 3.6. Side view of a fixed-free beam curling under stress.

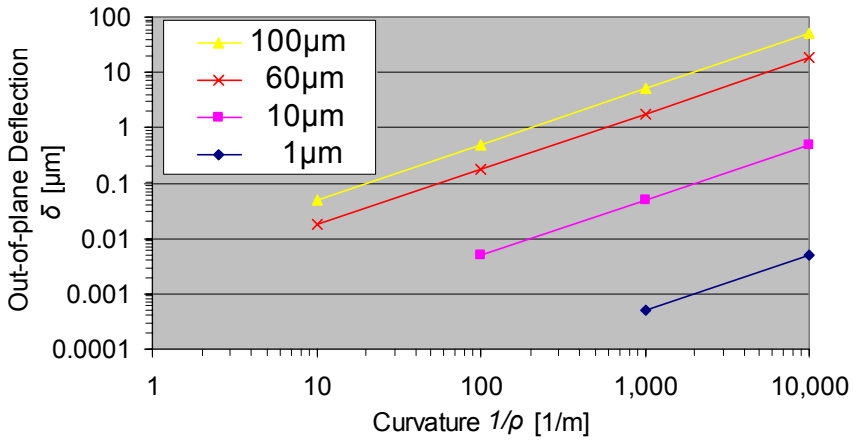

Figure 3.7. Graph of curvature vs. out-of-plane deflection for various beam lengths.

Out-of-plane deflection of the beams, δ, is the main consideration in this process because if $\delta > h$ the polymer will coat each beam, but the resulting membrane may not be flat or continuous. If $\delta \gg h$ then the membrane could have holes or could be fixed to the substrate by beams that curl very far out of plane. Functional problems could also develop from a non-flat membrane – the behavior of the device would be unknown. Due to these concerns, acceptable deflection and adequate flatness is defined as $\delta \leq h$. The relationship between δ, shown in Figure 3.6, given ρ and beam length, L (assuming $L \gg \delta$ and circular curvature) for a fixed-free beam is:

$$\frac{1}{\rho} = \frac{2\delta}{L^2 - \delta^2} \tag{5.4}$$

$$\delta \approx \frac{L^2}{2\rho} \tag{5.5}$$

Curvature as a function of δ is plotted in Figure 3.7. The longest beams in the mesh are 60 μm long. Therefore to keep the out-of-plane deflection no greater than mesh thickness, 0.11 μm, the curvature must be less than 61.1 m^{-1} or the radius of curvature must be greater than 16.4 x 10^{-3} m.

3.5. Test Setup

The "disk method" of stress analysis is used to characterize the material properties of the metals and oxides. In the disk method the material is deposited on a circular substrate; specifically, these tests use 3" and 4" <100> silicon wafers. Stress is determined from the difference in curvature of the substrate before and after material deposition according to Stoney's equation [19, 25]:

$$\sigma_{film} = \frac{M_{substrate} h_{substrate}^2}{6h_{film}} \left(\frac{1}{\rho_{with\_film}} - \frac{1}{\rho_{without\_film}} \right) \tag{5.6}$$

where M is biaxial elastic modulus of the wafer (related to E, but dependant on crystal orientation), $h_{substrate}$ is substrate thickness, h_{film} is substrate thickness, $\rho_{without\_film}$ is radius of curvature without the film, and ρ_{with_film} is radius of curvature with the film. M of the <100> silicon wafers is 180 GPa and $h_{substrate}$ varied for different batches of wafers between 0.381 mm to 0.600 mm. M was calculated based on the crystal orientation of the silicon [26]:

$$M_{substrate} = \frac{E}{1-\nu} \tag{5.7}$$

$$M(001) = C_{11} + C_{12} - \frac{2C_{12}^2}{C_{11}} \tag{5.8}$$

where E is Young's modulus, ν is Poisson's ratio, and C_{12} and C_{12} are components of the stiffness matrix for the <100> crystal orientation.

Certain assumptions are inherent in Stoney's equation:

- "The disc substrate is thin and has transversely isotropic elastic properties with respect to the film normal.
- The applied film thickness is much less than the substrate thickness.
- The film thickness is uniform.
- Temperature of the disk substrate/film system is uniform.
- Stress is equi-biaxial and homogeneous over the entire substrate.
- Film stress is constant through the film thickness." [19]

Specific discrepancies between the assumptions and the test setup are that the material was not uniformly thick across the wafer and its stress is probably not uniform either.

3.6. Curl measuring test setup[†]

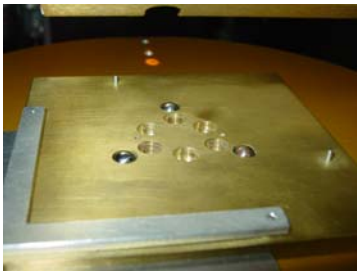

Figure 3.8. 3-point mount for curl measurement. The L-bracket aligns the wafer and the three ball bearings support the wafer at three points.

Figure 3.9. Illustration of the δ measurement convention.

3" and 4" silicon wafers were mounted on a 3-point mount shown in Figure 3.8. The Tencor profilometer scanned the center of the wafer for length, L = 1.5 cm. δ was measured as the difference between the edge and center of the wafer as illustrated in Figure 3.9.

3.7. Oxide Stress Data

Stress and thickness are measured for spin-on glass (SOG) and thermal oxide. SOG type 31F is purchased from Filmtronics, Inc. [102]. To prevent degradation, the SOG is stored under refrigeration and removed to ambient temperature 8-24 hours before use. To deposit the SOG, the wafer is mounted in a spinner and 2-3 ml of SOG is applied. The spinner program has a spread step of 300 rpm for 5 seconds and a spin step of 3000 rpm for 30 seconds. Next, the wafer is soft-baked at 80ºC for 1 minute, 150ºC for 1 minute, then hard-baked 400ºC for 1 hour. The experiments used 4" test grade bare silicon wafers.

To measure oxide thickness two approaches are used. The oxide is measured with the Nanometrics interferometer which measures thickness of transparent materials.

[†] Winnie Yu provided the curl characterization test setup. Thanks.

Thickness is also measured by masking part of the wafer with Kapton tape during a BHF etch. The tape protected part of the oxide to produce a measurable step.

The SOG has a thickness of 3800 Å and a tensile stress of about +100 ±10 MPa. Various parameters affect the thickness and stress of the SOG including spin speed, spin time, bake temperature, bake time, and the age of the SOG.

Different wafers with thermal oxide are used; the oxide is grown by the wafer manufacturer, Silicon Quest, to a specified thickness [103]. The two samples tested are 3" and test grade wafers with 350 Å oxide and 4" prime grade wafers with 10,000 Å oxide. Oxide thicknesses of 350 Å and 10,000 Å have about the same compressive stress of -400 ±10 MPa. This is much greater than the compressive -20 to -40 MPa value listed by Madou [19].

3.8. Metal Stress Data

Unlike the oxides, stress in the metal is more directly controllable. Aluminum and platinum are sputtered in a Kurt J. Lesker sputtering machine[‡] with control over the deposition time, pressure, gas, DC power, and distance between target and substrate. Another important factor in metal sputtering is the underlying layer. For example, metal sputtered on silicon has different properties than metal on thermal oxide.

To analyze aluminum's material properties, two experiments are conducted where the constants were a sputtering power of 100 W, argon gas, and fixed target to substrate distance of 3½" on 3" test grade bare silicon wafers. In the first aluminum experiment, time is varied and pressure kept constant at 5 mTorr; in the second experiment pressure is varied and time was constant at 19 minutes. To measure metal thicknesses a simple lift-off[§] technique is used. The wafer was written on with a Sharpie™ marker before sputtering. After sputtering, the marker lifts off in an acetone ultrasonic bath. The result is a clean step to measure film thickness. The test setup for metal stress measurement is the same as for the oxide.

[‡] George Lopez Subrebost helped me extensively with the Lesker. Thanks.
[§] Matt Moneck taught me the Sharpie™ lift-off technique. Thanks.

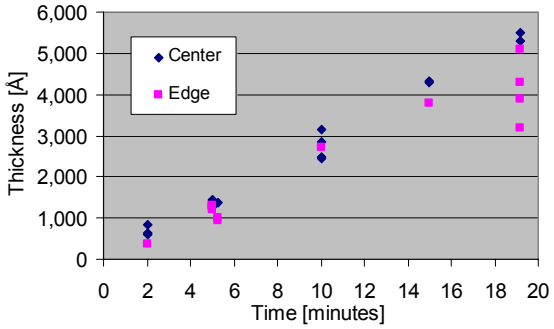

Figure 3.10. Aluminum: Deposition time vs. Film thickness for constant pressure of 5 mTorr. Measurements were taken at the center of the wafer and edge. All data point taken at a specific time correspond to one wafer, except for 5 minutes and 10 minutes where there is data from two wafers.

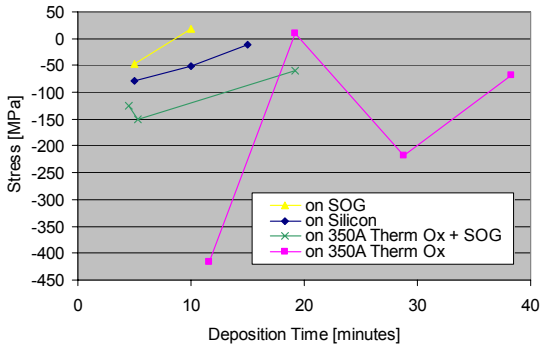

Figure 3.11. Aluminum: Deposition time vs. stress for constant pressure of 5 mTorr. The underlying layer varied as indicated in the legend. All values are ±10 MPa.

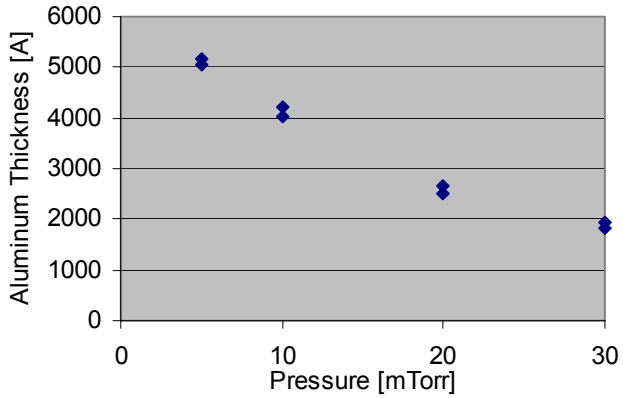

Figure 3.12. Aluminum: pressure vs. film thickness at wafer center for constant time of 19 minutes.

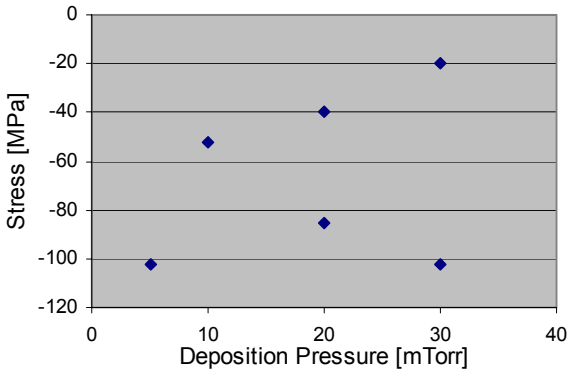

Figure 3.13. Aluminum: Deposition pressure vs. film stress for constant time of 19. All values are ±10 MPa.

Figure 3.10 shows that the relationship between deposition time and film thickness is linear; however, the deposition rate at the edge of the wafer is different than that at the center. The positive linear relationship between deposition time and stress is shown in Figure 3.11.

Figure 3.12 and Figure 3.13 show the results from the second aluminum experiment where pressure varied and time was constant. Figure 3.12 shows an approximately linear relationship between deposition pressure vs. thickness. There is no clear trend between deposition pressure and stress plotted in Figure 3.13.

In the platinum experiments the constant conditions are: power of 75 W, time of 2.5 minutes, argon gas, and fixed target to substrate distance of 3½" on 3" test grade bare silicon wafers. The argon pressure varied in the platinum experiments. The platinum is different from the aluminum in that processing pressure does not affect film thickness – it is always about 1100 Å.

Most of the data was taken on "test grade" silicon wafers which produced rather variable results; the out-of-plane deflection, δ, values which were used to determine stress generally varied by ±75 Å, resulting in an error of about ±10 MPa. To compensate

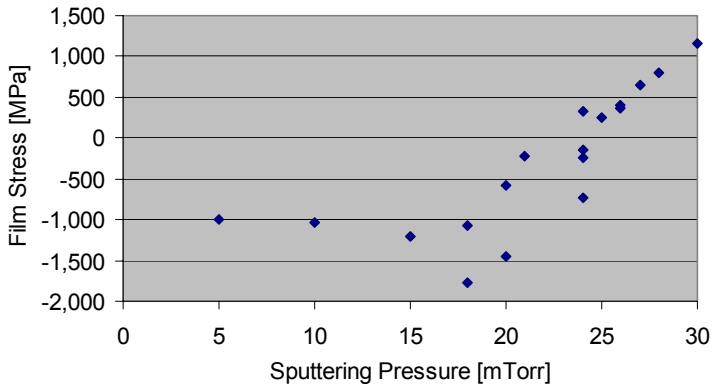

Figure 3.14. Platinum sputtering pressure vs. film stress. All values are ±10 MPa.

for the variation, 3 to 5 δ measurements were averaged for each wafer. Only the final batch of wafers with 10,000 Å thermal oxide were "prime grade" wafers. The difference was dramatic: the δ values from the prime wafers only varied by ±10 Å corresponding to an error of about ±1 MPa.

Another major difference from aluminum is that the platinum has a chromium cladding layer of 50 Å. The chromium is deposited for 20 seconds at a power of 100 W, argon gas at a pressure of 5 mTorr, and fixed target to substrate distance of 3½". The chromium helps to better adhere platinum to the material below as well as aiding in lift-off. Figure 3.14 shows stress vs. sputtering pressure for platinum without the chromium cladding layer; however, tests showed no significant change in platinum stress with or without the chromium.

The result from the aluminum and platinum experiments is that neither material was found to have stable stress characteristics from run to run. The aluminum stress was very erratic with varying pressure. The platinum stress was close to linear from 20 to 30 mTorr, but when a pressure of 24mTorr is applied to get a film stress close to 0 MPa the stress varies from -720 MPa to +330 MPa. Without stable stress control for the metal layer, curl matching proves impossible for the beams.

3.9. Patterning Silicon

Another concern in the fabrication is patterning the bulk silicon. Two solutions are proposed: "etch lag effects" and "selective etching". All of the effects that contribute to uneven bulk etching, such as Aspect-Ratio Dependent Etching (ARDE) and

microloading, are referred to here as ‘etch lag effects’. Selective etching is where parts of the silicon are protected for part of the silicon etch resulting in a varying profile.

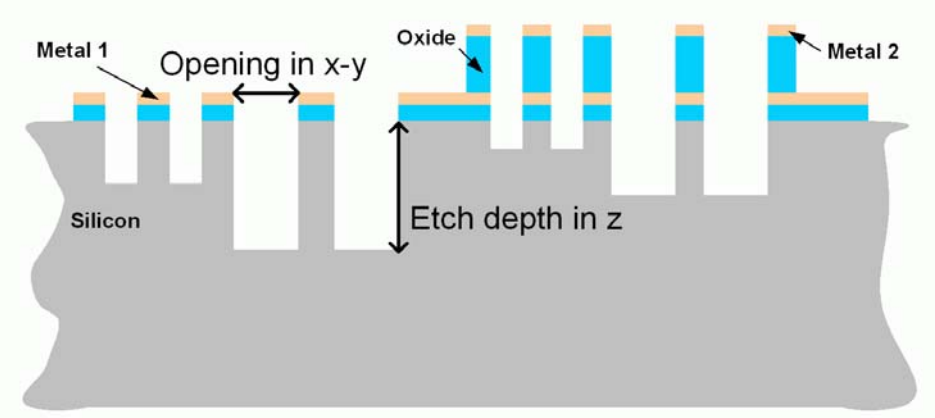

Figure 3.15. Diagram of ARDE shown in cross section. As the aspect ratio increases (height in z to opening in x) the etch decreases for the same etching conditions.

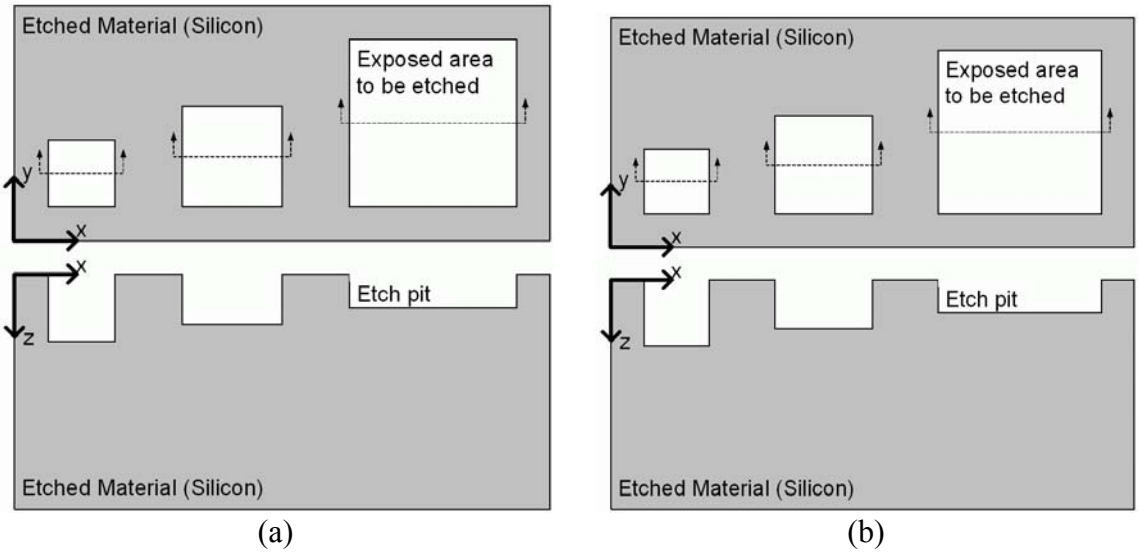

Figure 3.16. (a) Diagram of microloading from features size. (b) Diagram of microloading from pattern density. The dashed lines indicate where the x-z profile is taken.

Bourouina describes how to bulk micromachine nearly arbitrary shapes in silicon with etch lag effects [27]. When etching silicon, three different etching effects occur: ARDE, also known as RIE lag, microloading from pattern density, and microloading from feature size respectively depicted in Figure 3.15, Figure 3.16(a), and Figure 3.16(b).

In the ARDE phenomenon, as aspect ratio increases etching becomes more difficult. This is thought to occur because reactive species have a harder time reaching the material. ARDE causes smaller features to etch more slowly than larger ones because as the etch goes deeper, the aspect ratio of the smaller features increases more quickly

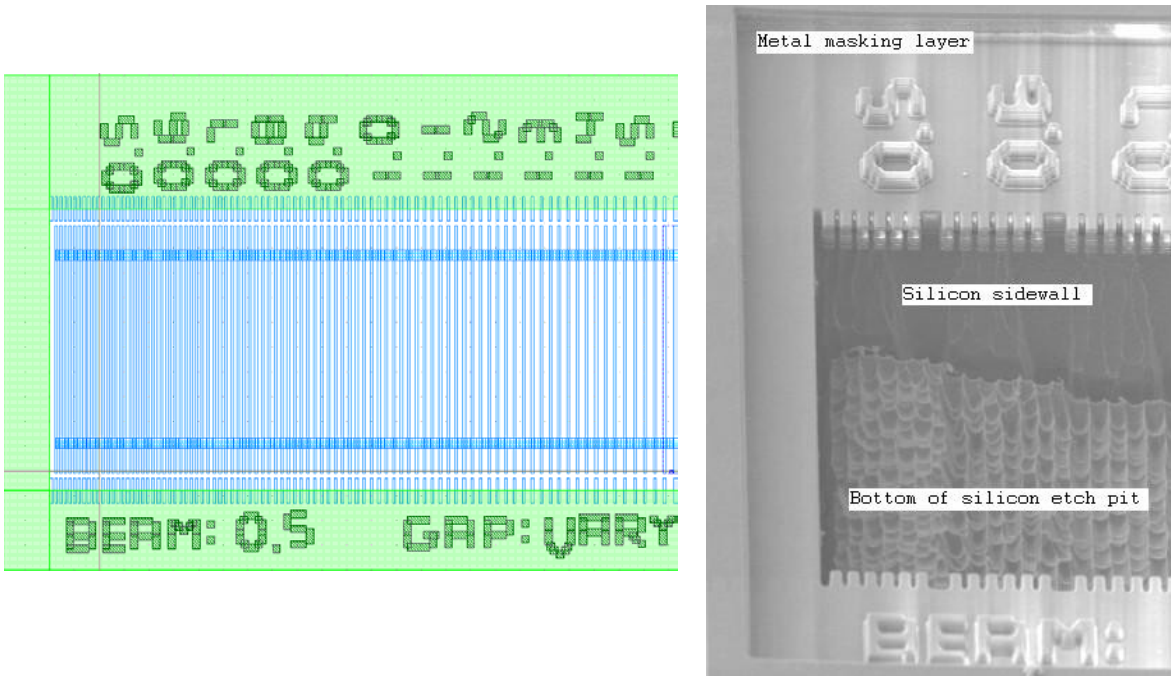

(a) (b)

Figure 3.17. (a) Layout for the etch lag test structure. The vertical blue lines are 0.5 μm metal beams. The numbers above the beams indicate the gap width between the beams in microns. (b) Scanning Electron Microscope (SEM) picture of the fabricated test structure. The chip was mounted at 45° so the side wall is visible. The increasing depth of the side wall shows the increasing etch depth due to the etch lag effects as the gaps between the beams increased from 0.5 μm to 0.7 μm.

than for the larger features. This also means that as etches go deeper their rate will slow due to increasing aspect-ratio. ARDE becomes more prominent the deeper the etch goes.

In microloading, increasing the amount of area to be etched slows down etch rates "which is mainly due to local depletion of etchant" [27]. So in microloading from pattern density, a single isolated feature will etch faster than a cluster of the same feature as in Figure 3.16(b). This also means that larger features will etch more slowly than small features because of the local depletion of etchant as in Figure 3.16(a) – referred to as microloading from feature size. So, ARDE and microloading act in different ways due to different phenomena. Etch lag effects are a combination of these phenomena which with careful design can be utilized to create a desired shape.

To analyze the etch lag effects four test structures are created of 0.5 μm beams with varying gaps from 0.50 μm to 2.5 μm. Figure 3.17(a) is part of the layout where 50 μm long beams were laid out in parallel with two cross beams linking all the beams together. CMOS fabrication was done by Taiwan Semiconductor Manufacturing

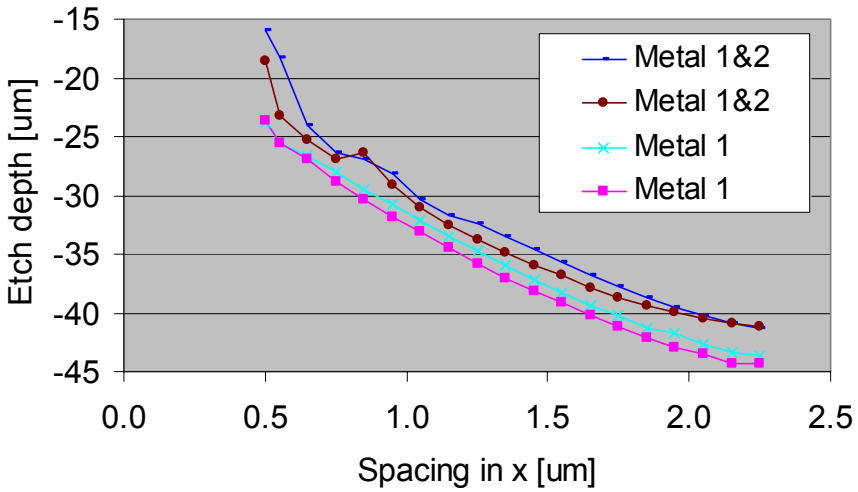

Figure 3.18. Graph of silicon profile from the etch lag test structure. The beams that masked the silicon were of two different heights: two test structures had beams of metal 1 only, two other test structures had beams of metals 1 and 2 which increased their aspect ratios corresponding to a shallower etch.

Company (TSMC) in their 4-metal 0.35 µm CMOS process and the post-CMOS oxide etch and silicon etch were performed at Carnegie Mellon[**]. The oxide etch exposed the metal and silicon. The metal beams masked the silicon during the silicon etch. The varying distance between the beams varied the aspect ratio and exposed area of the silicon. To further test the effect of aspect ratio, two of the test structures had beams of only metal 1 and the other two had beams of metals 1 and 2. These etch lag effects varied the etch rate of the silicon and caused a variable profile. To measure the depth of the silicon, the masking beams are removed by pulling up the cross beams. Figure 3.17 (b) shows the fabricated device after the metal mask has been removed and the measured profile is shown in Figure 3.18.

[**] Jay Brotz did the post-CMOS micromachining on these chips, since the test structures were on the same chips as his devices. Thanks. The recipe can be found in Stillman [28].

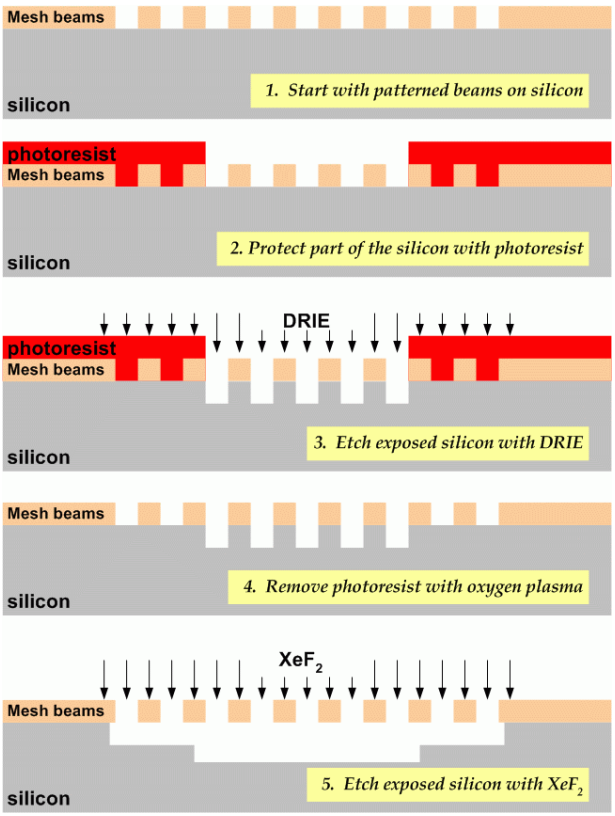

Figure 3.19. Diagram of selective etching.

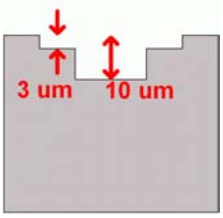

First etch:
10 Cycles DRIE
Second etch:
8 Cycles XeF_2

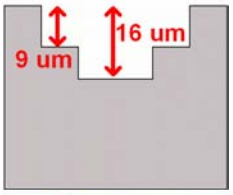

First etch:
10 Cycles DRIE
Second etch:
20 Cycles XeF_2

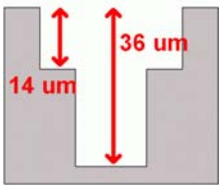

First etch:
30 Cycles DRIE
Second etch:
30 Cycles XeF_2

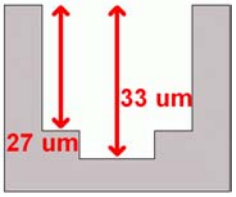

First etch:
10 Cycles DRIE
Second etch:
40 Cycles XeF_2

Figure 3.20. Cross-section profiles of silicon from selective etching. A part of the silicon is exposed to DRIE, then all the silicon is exposed to the XeF2 etch. These depths are for a 500 μm diameter pump.

Figure 3.19 shows the process flow for selective etching where a protective photoresist mask covers part of the exposed silicon during the silicon etch. After an initial deep reactive ion etching (DRIE) silicon etch the photoresist is removed with an oxygen plasma. An isotropic XeF_2 then completes the silicon etching. The result is a two-tiered silicon profile. Schematic cross-sections from the process flow in Figure 3.19 are presented in Figure 3.20 for open pits without a mesh covering them.

3.10. Final Design

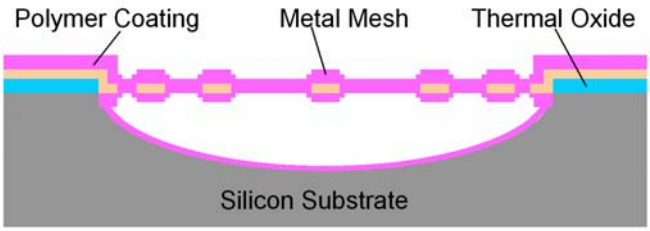

Figure 3.21. Cross-section of the fabrication process of the microvalve. The substrate is patterned to different depths and the mesh beams are only made of metal.

After analysis of materials and processing techniques, the final process flow consists of platinum on thermal oxide on a 3" silicon wafer. The final design eliminates the oxide layer from the mesh and uses it only to insulate the anchors because this circumvents the stress matching problem which proved untenable. The use of only platinum for the microstructures was intended to eliminate the vertical stress gradient in the mesh beams that causes them to curl. The spring-like design of the mesh mitigates against axial stress by allowing lateral beam bending.

In the final design, a metal mesh is suspended over a silicon cavity and anchored to thermal oxide at its edges as in Figure 3.21. Oxide electrically isolates the metal mesh where the mesh is anchored to the silicon. Polymer insulates the mesh where it lies above the silicon pit. A further benefit of this design is that eliminating the oxide in the mesh reduces the gap between the metal and the silicon, greatly reducing the pull-in voltage [12].

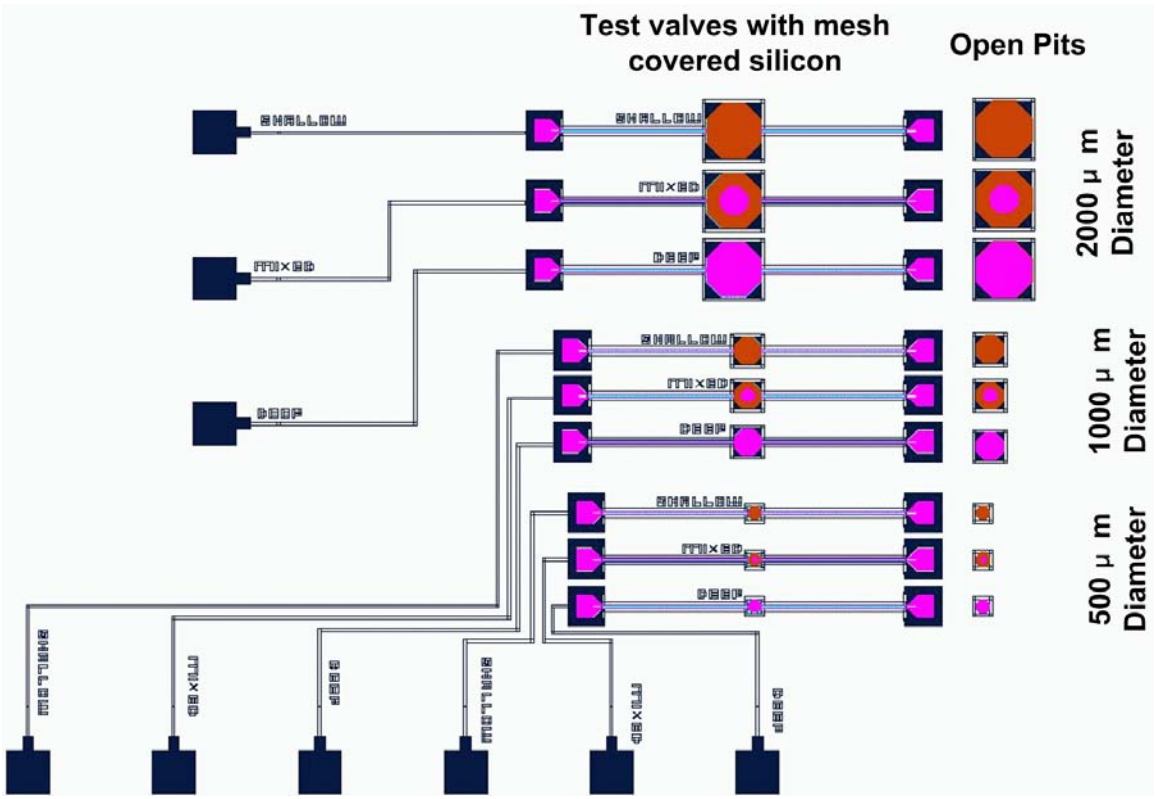

Figure 3.22. Layout of test devices with mesh and open pits without mesh. The devices have diameters of 500, 1000, or 2000 µm and silicon profiles are SHALLOW, MIXED, or DEEP.

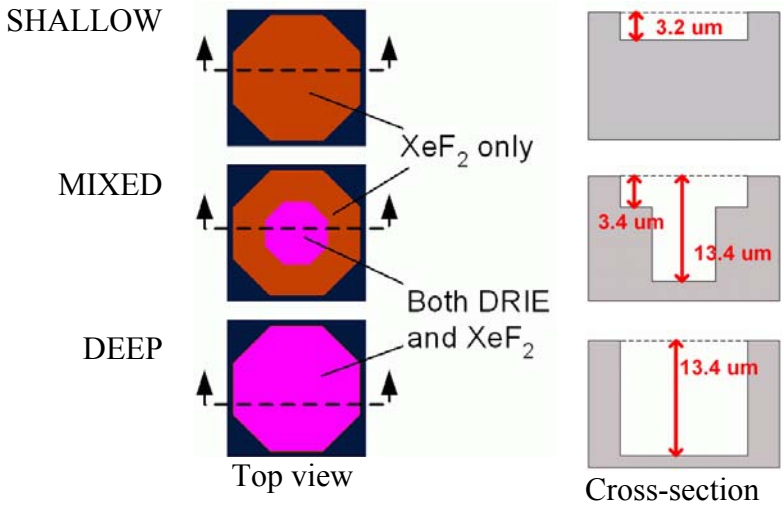

Figure 3.23. The top view shows a detailed view of three 500 um diameter open pits from Figure 3.22. Cross-section view of etch results. The etch recipe was 10 cycles of DRIE and 8 cycles of XeF_2.

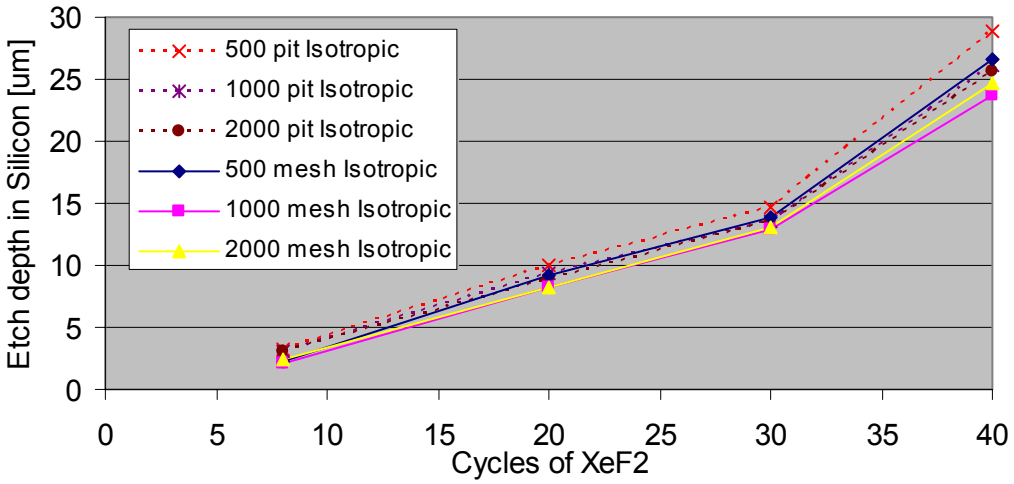

Figure 3.24. Graph of silicon etch depth vs. number of cycles of xenon diflouride for uncovered, 'pit', and mesh covered, 'mesh', pits of different diameters.

In the test device design there are two main variables: membrane diameter and silicon depth. The layout of the test wafer shown in Figure 3.22 has 9 test devices – one for each combination of diameter and silicon etch. Although the membranes are modeled as circular, they are fabricated as octagons. The layout also has 9 open pits also corresponding to the combination of diameter and silicon etch. The actuating membrane diameter is either 500 µm, 1000 µm, or 2000 µm. The other variable is silicon depth which is categorized as SHALLOW, DEEP, or MIXED. The SHALLOW profile is only exposed to the XeF_2 step of silicon etching. The DEEP profile is exposed to both the DRIE and XeF_2 step of silicon etching. The inner part of the MIXED membrane is exposed to the DRIE etching but the outer part is not. All of the MIXED area is exposed during the XeF_2 step, resulting in a two-tiered silicon profile (see Figure 3.23).

Open pits are used as test structures to compare with the mesh covered pits. Data taken by a Dektak profilometer from scans of the open pits and mesh covered pits with the mesh removed is plotted in Figure 3.24. The open pits etch faster than their mesh covered counterparts; nonetheless, they are a good reference for etch depth.

4. EXPERIMENTAL RESULTS

All of the fabricated devices use the same recipe for the oxide and metal layers, but the silicon etch times vary for each device[††]. The substrates used for the test devices are 4" p-doped 500 μm thick prime grade silicon wafers with 10,000 Å thermal oxide purchased from Silicon Quest International, Inc. [103]. For each layer there is a corresponding mask[‡‡]: an OXIDE mask which makes holes in the oxide to expose the silicon below; a METAL mask to pattern the metal; and a DEEP mask which protects parts of the exposed silicon during the DRIE silicon etch and is removed before the XeF_2 etch to create the two-tiered silicon profile.

The thermal oxide is patterned with a 30-minute BHF etch. The next step is the metal deposition where a 50 Å chromium cladding layer is sputtered at 100 W for 20 seconds at 5 mTorr. Next 1100 Å of platinum is sputtered at 75 W for 2.5 minutes. The metal is patterned using the lift-off technique. The repeating cells of the metal mesh are 60 μm x 60 μm with 3 μm beams with 3 turns and 3 μm spacing between beams. An ultrasonic acetone bath lifts off the photoresist and the excess metal that sits on it, thus patterning the metal. The final processing step etches the silicon and releases the metal mesh. The silicon etch has two parts to create the two-tiered profile. A photoresist mask, called the 'DEEP' mask, protects some of the exposed silicon during a directional DRIE etch. The DEEP mask is removed with an oxygen plasma since an acetone bath would damage the etched silicon structures. Finally, an isotropic XeF_2 etch undercuts the silicon and releases the metal mesh. The number of cycles of DRIE and XeF_2 varied as indicated in the experiments. Three different versions of the masks (OXIDE, METAL, and DEEP) were used but the process flow is kept constant for all.

[††] Refer to Appendix D for a detailed description of the process recipe.
[‡‡] Refer to Appendix C for mask designs.

4.1. Materials Characterization

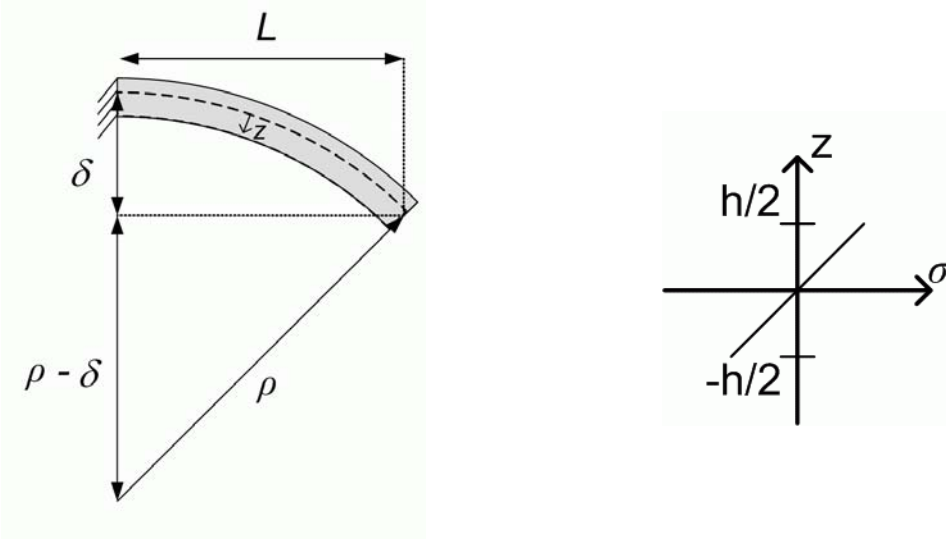

(a) Diagram of bending beam (b) Graph of stress vs. z

Figure 4.1. Beam curving in (a) due to a stress gradient as shown in (b). Figure based on [29].

The stress gradient is characterized with a simple fixed-free beam test structure since the curvature of the material is such a major concern in the design. The curvature of a fixed-free beam test structure indicates the stress gradient in the metal beams. From Senturia, the stress gradient in *z* for the fixed-free beam in Figure 4.1 is [29]:

$$\frac{d\sigma_x}{dz} = -\frac{E}{\rho} \tag{4.1}$$

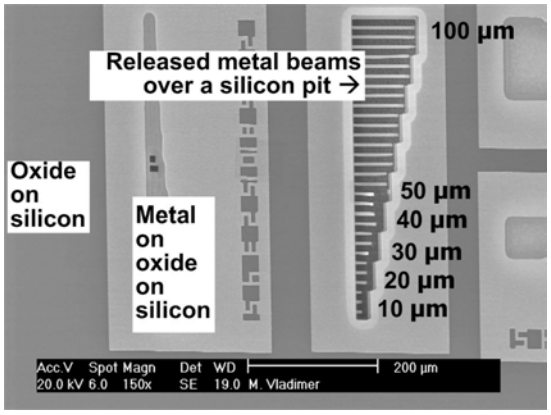

Figure 4.2. SEM picture of the fixed-free beam test structure used to determine curl. The numbers alongside the groups of beam indicate beam length. The labels indicate the material layers below.

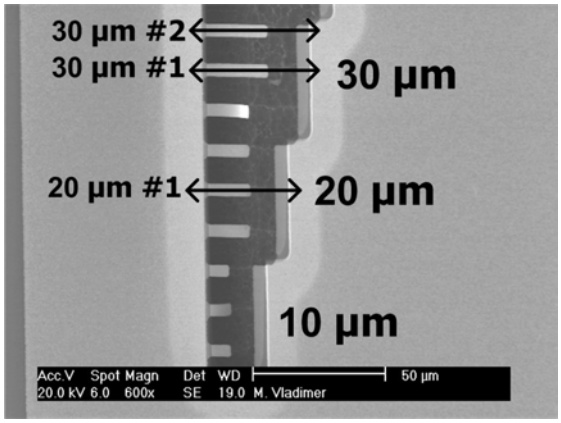

(a) Detail of beams 10 µm to 30 µm

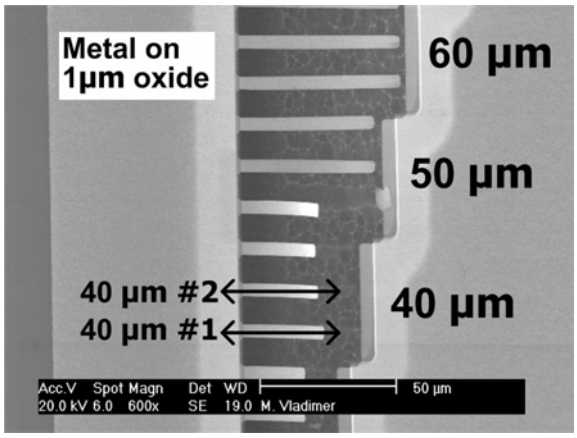

(b) Detail of beams 40 µm to 60 µm

Figure 4.3. Detailed view of the test structure. The numbers alongside the groups of beam indicate beam length. The specifically numbered beams have been measured. The lines across certain beams indicate the scan line used.

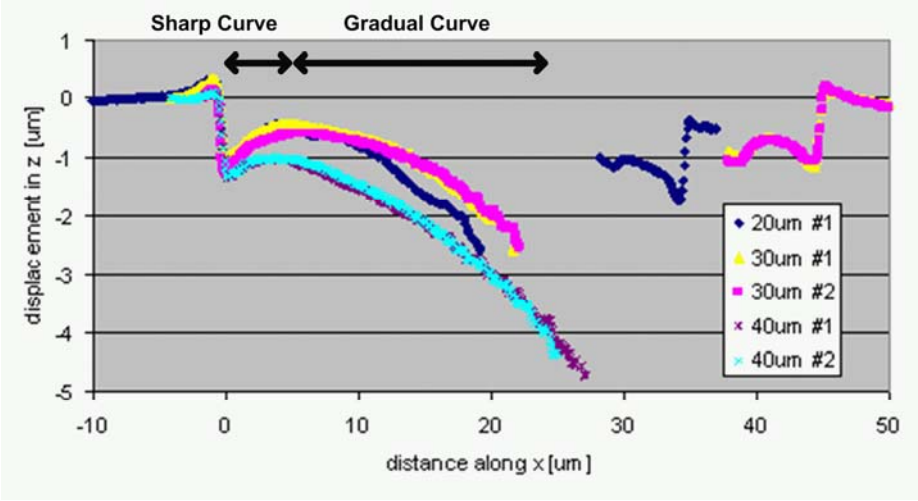

Figure 4.4. Graph of displacement in z along the length of the beam for fives beams from 20 µm to 40 µm long. The data corresponds to the beams labeled in Figure 4.2. The data was taken with a Wyco interferometer.

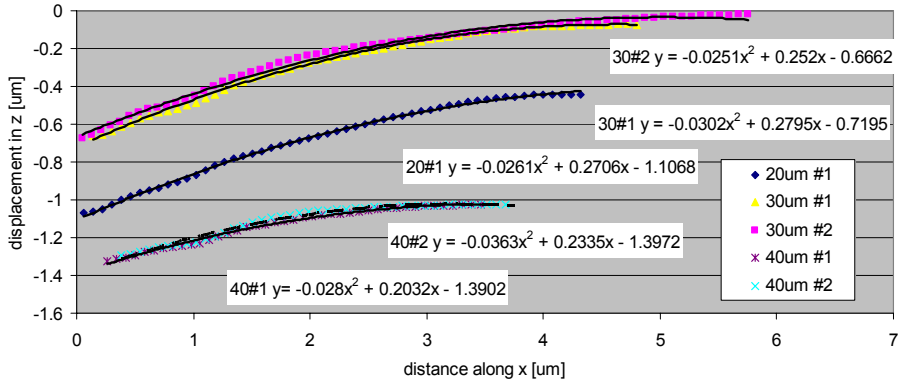

Figure 4.5. Detail of the graph in Figure 4.4 showing the sharp part of the curve. The equations shown are quadratics curve fit to each set of data.

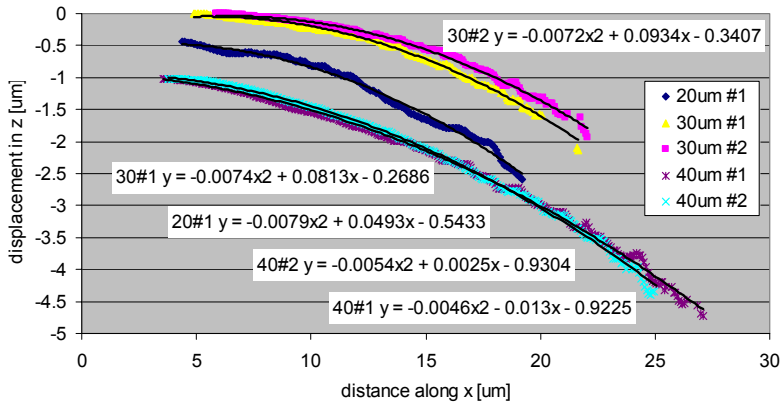

Figure 4.6. Detail of the graph in Figure 4.4 showing the second part of the curve. The equations shown are quadratics curve fit to each set of data.

Figures 4.2 and 4.3 are pictures of the test devices and Figure 4.4 is the z deflection of the beam vs. the length of the beam. The beams are fabricated in the same process as the mesh and received 2 cycles of DRIE and 50 cycles of XeF_2. The beam has a region of sharp curl shown in Figure 4.5 and more gradual curl shown in Figure 4.6. The lines drawn on the beams in Figure 4.3 correspond to the data taken in Figure 4.4. The beams are optically verified as not touching the silicon using a Wentworth probe station. For the 20 µm and 30 µm beams in Figure 4.4 the scans begin on platinum on oxide. A 1 µm step shows where the oxide is etched and the platinum touches down to the silicon before release. The scan lines then trace the beam as it curves in z. Next there is a metal lip overhanging the silicon pit opposite the beams. Finally, the scan returns to metal on 1 µm thick oxide. The data for the 20 µm beam has a leveling error since the metal on oxide should be at 0 µm displacement on both sides of the pit. The beams are considered to have two regions of curvature: sharp and gradual as labeled in Figure 4.4.

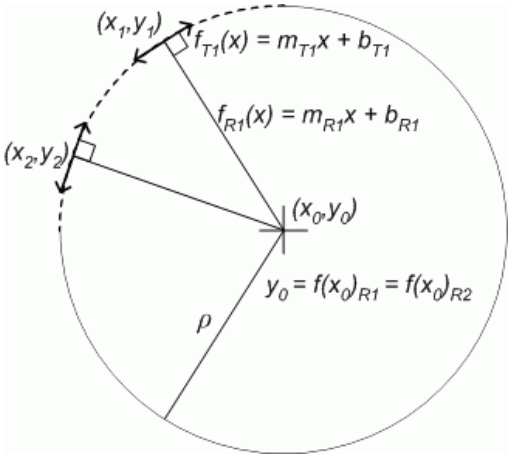

Figure 4.7. The data points of the bent beams are represented by the dotted portion of the circle.

To calculate the curl of the beams, the data sets are considered to be arcs on a circle as shown in Figure 4.7[§§]. To extract the radius of curvature of the data, two points at the ends of the arc are examined, (x_1, y_1) and (x_2, y_2). Tangent lines $f_{T1}(x)$ and $f_{T2}(x)$ are drawn with the equation (analysis is shown only for f_{T1}, but it is the same for both):

$$f_{T1}(x) = m_{T1}x + b_{T1} \tag{4.2}$$

To get the slope of the line at the point (x_1, y_1), the derivative of the curve-fit quadratic equation shown in Figure 4.5 and Figure 4.6 is used:

$$y = Ax^2 + Bx + C \tag{4.3}$$

$$m_{T1} = \frac{dy}{dx} = Ax_1 + B \tag{4.4}$$

Next, $f_{R1}(x)$, a line perpendicular to the tangent, hence along the radius, is drawn also through point (x_1, y_1). The slope of this line is found by:

$$m_{R1} = \frac{-1}{m_{T1}} \tag{4.5}$$

Given the slope of the line and that it goes through point (x_1, y_1) the y-intercept is determined:

$$b_{R1} = y_1 - \left(\frac{-1}{m_{T1}}\right)x_1 \tag{4.6}$$

Thus the equations for $f_{R1}(x)$ and $f_{R2}(x)$ are solved. Setting them equal to each other determines the x-coordinate of the center of the circle:

$$\frac{-1}{m_{T1}}x_0 + b_{R1} = \frac{-1}{m_{T2}}x_0 + b_{R2} \tag{4.7}$$

[§§] Fang Chen helped in this analysis. Thanks.

Table 4.8. Calculation of curvature and stress gradient for the sharply curving part of the beam [30].

	X1	Y1	m1	b'1	x0	y0	ρ[m]	E_{Pt} [Pa]	$d\sigma_x/dz$ [Pa/m]
20 μm #1	0.38	-1.00	0.26	-1.10	0.00	-1.09	0.40	1.68E+11	4.22E+11
30 μm #1	0.30	-0.64	0.27	-0.72	0.00	-0.72	0.31	1.68E+11	5.43E+11
30 μm #2	0.45	-0.56	0.24	-0.67	0.00	-0.66	0.46	1.68E+11	3.63E+11
40 μm #1	1.30	-1.18	0.17	-1.39	0.00	-1.39	1.32	1.68E+11	1.27E+11
40 μm #2	1.42	-1.15	0.18	-1.41	0.00	-1.44	1.45	1.68E+11	1.16E+11

	X2	Y2	m2	b'2	x0	y0	ρ[m]	E_{Pt} [Pa]	$d\sigma_x/dz$ [Pa/m]
20 μm #1	3.84	-0.45	0.17	-1.11	0.00	-1.09	3.89	1.68E+11	4.31E+10
30 μm #1	4.64	-0.07	0.14	-0.72	0.00	-0.72	4.68	1.68E+11	3.59E+10
30 μm #2	5.03	-0.03	0.13	-0.67	0.00	-0.66	5.07	1.68E+11	3.31E+10
40 μm #1	3.39	-1.02	0.11	-1.39	0.00	-1.39	3.41	1.68E+11	4.93E+10
40 μm #2	3.51	-1.02	0.11	-1.40	0.00	-1.44	3.53	1.68E+11	4.76E+10

Table 4.9. Calculation of curvature and stress gradient for the gradually curving part of the beam [30].

	X1	Y1	m1	b'1	x0	y0	ρ[m]	E_{Pt} [Pa]	$d\sigma_x/dz$ [Pa/m]
20 μm #1	7.62	-0.63	-0.01	-0.54	0.00	-0.52	7.62	1.68E+11	2.21E+10
30 μm #1	11.30	-0.30	0.00	-0.27	0.00	-0.25	11.30	1.68E+11	1.49E+10
30 μm #2	11.22	-0.22	0.01	-0.36	0.00	-0.37	11.22	1.68E+11	1.50E+10
40 μm #1	7.41	-1.27	-0.05	-0.92	0.01	-0.73	7.42	1.68E+11	2.27E+10
40 μm #2	7.61	-1.21	-0.04	-0.92	0.00	-0.90	7.61	1.68E+11	2.21E+10

	X2	Y2	m2	b'2	x0	y0	ρ[m]	E_{Pt} [Pa]	$d\sigma_x/dz$ [Pa/m]
20 μm #1	18.22	-2.25	-0.09	-0.52	0.00	-0.52	18.30	1.68E+11	9.18E+09
30 μm #1	20.06	-1.60	-0.07	-0.25	0.00	-0.25	20.11	1.68E+11	8.36E+09
30 μm #2	21.02	-1.58	-0.06	-0.37	0.00	-0.37	21.05	1.68E+11	7.98E+09
40 μm #1	24.52	-3.89	-0.13	-0.80	0.01	-0.73	24.71	1.68E+11	6.80E+09
40 μm #2	23.92	-3.94	-0.13	-0.91	0.00	-0.90	24.11	1.68E+11	6.97E+09

Thus:

$$x_0 = \frac{b_{R1} - b_{R2}}{1/m_{T1} - 1/m_{T2}} \tag{4.8}$$

Plugging the x_0 value back into the $f_{R1}(x)$ and $f_{R2}(x)$ determines the $y_0 = f_{R1}(x)$ value. Finally calculated is the radius of the circle – the distance between the center point (x_0, y_0) and the points on the circumference (x_1, y_1) and (x_2, y_2):

$$\rho = \sqrt{(x_1 - x_0)^2 + (y_1 - y_0)^2} \tag{4.9}$$

Since the values of (x_1, y_1) and (x_2, y_2) are crucial to determining the radius, the data points chosen were as close as possible to the curve-fit line. The results for the first curve are shown in Table 4.8 and the results for the second curve are shown in Table 4.9. The results in Table 4.8 show a stress gradient between $40*10^9$ and $200*10^9$ Pa/m for the

sharp curve. The results in Table 4.9 show a stress gradient between $8*10^9$ and $20*10^9$ Pa/m for the gradual curve. The data for the gradually curving part of the beam are more accurate probably because it is over a longer distance and the data are more consistent.

4.2. Device Fabrication

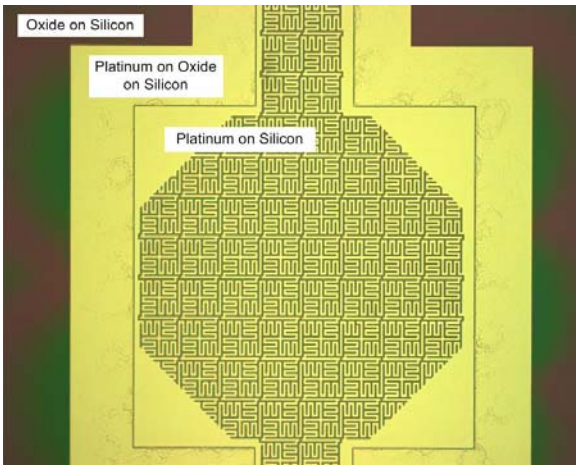

Figure 4.10. Microscope picture taken at 20x of a 500 µm diameter pump taken after platinum patterning and lift-off.

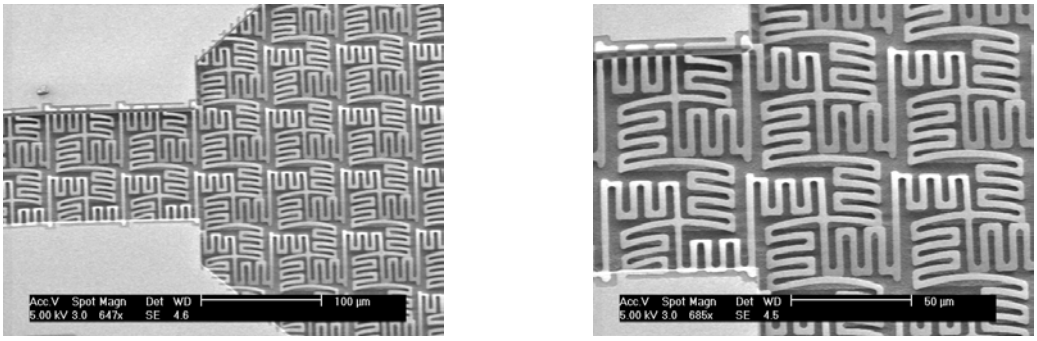

(a) Channel to membrane connection (b) Detail of connection

Figure 4.11. SEM pictures of a 500 µm diameter membrane where the silicon has been etched to a depth of approximately 8 µm. Device shown is from *Wafer K*.

Figure 4.10 shows an octagonal mesh with two channels in the middle of the process flow, after platinum patterning but before the silicon etch. The mesh is anchored by a wide band of platinum on thermal oxide on silicon. Outside the platinum band is oxide on silicon. The gaps in the mesh expose the underlying silicon.

After the devices are released, pictures are taken with the SEM. All SEM pictures are taken with the substrate tilted 30º. Figure 4.11 shows the junction where the mesh-covered channel connects to the octagonal mesh over a pit in the silicon approximately 8 µm deep. The silicon profile is never perfectly flat so all depth measurements are

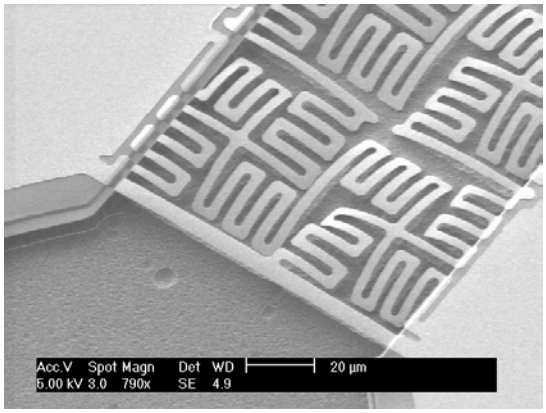

Figure 4.12. SEM picture of a channel to port connection where the silicon has been etched to a depth of approximately 8 µm. Device shown is from *Wafer K*.

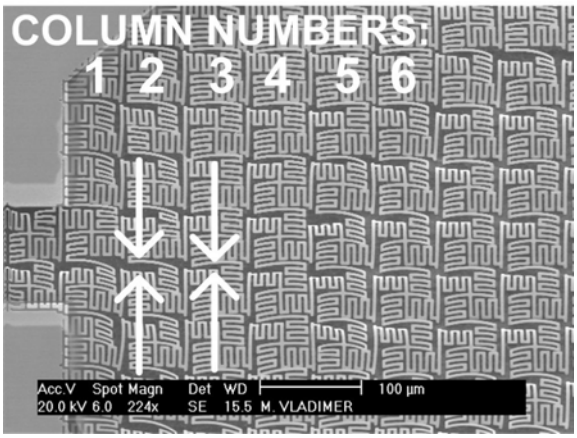

Figure 4.13. A MIXED 1000 µm diameter membrane where the SHALLOW depth is 25 µm and the DEEP depth is 31 µm. Device shown is from *Wafer K*.

approximate. Figure 4.12 shows the junction at the other end of the channel where it connects to a port. The 120 µm cross-bar that ends the channel does not significantly buckle out of plane, which indicates that there is not a large amount of axial stress in the platinum. Although the mesh was expected to lie flat, it clearly doesn't. All of the released devices have this problem. Figure 4.11 (b) and Figure 4.12 show that the mesh curls down to the substrate.

Figure 4.13 shows a 1000 µm diameter mesh where the outer ring of silicon is etched to a SHALLOW depth of 24 µm and the deeper inner circle of silicon is at a DEEP depth of 31 µm. The profile is achieved by etching for 10 cycles of DRIE and 40

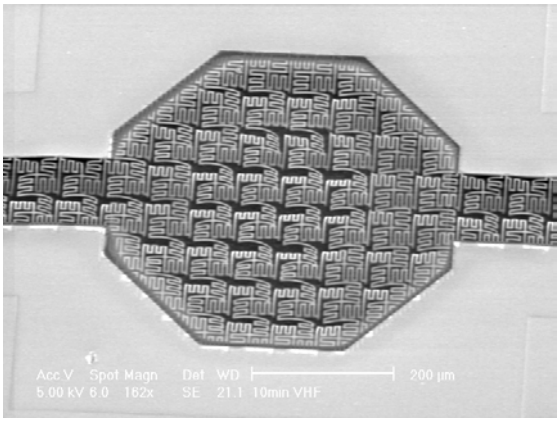

(a) outer SHALLOW depth of 28 µm
inner DEEP depth of 34 µm

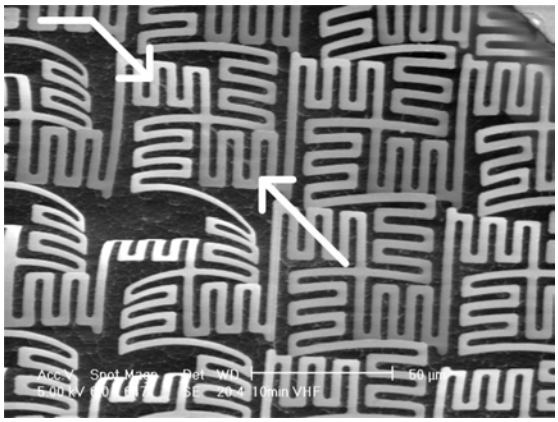

(b) detail of (a)

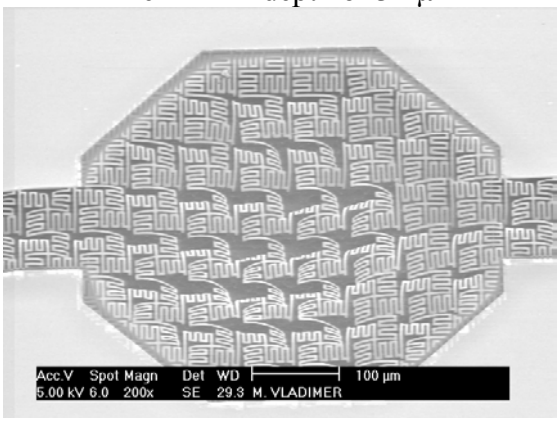

(c) outer SHALLOW depth of 50 µm
inner DEEP depth of 50.4 µm

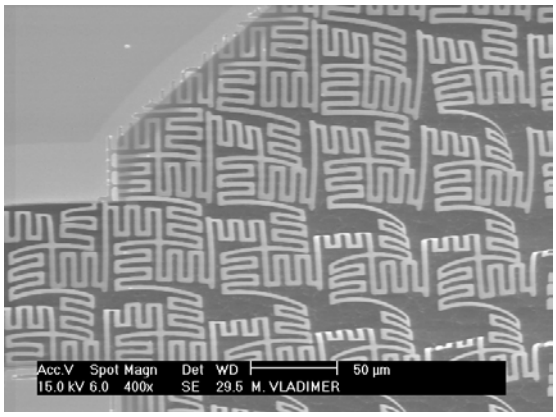

(d) detail of (d)

Figure 4.14. The same MIXED 500 µm diameter membrane before and after a 60 cycle XeF_2 etch. The arrows in (b) show the lip between the DEEP and SHALLOW region. Device shown is from *Wafer K*.

cycles of XeF_2. The depth measurements were made by removing the mesh and measuring with a Dektak stylus profilometer. The figure shows that the beams still bend down and touch the silicon. It also illustrates how the mesh conforms to the substrate. In Figure 4.13, the first two columns of repeating mesh cells bend more than their neighbors in columns 3 and 4 which is shown by the appearance of larger gaps between the cells as indicated by the arrows. Inferred from this is that the third and fourth columns are already in contact with the silicon – and so the gaps between the cells appear smaller. Again at the transition from SHALLOW region to DEEP region in columns 5 and 6 the gaps between the cells increases (Figure 4.13).

Figure 4.14 shows a 500 µm diameter mesh bending to cover the substrate. In Figure 4.14 (a) the outer ring of the silicon has a SHALLOW depth of 28 µm and the inner DEEP depth is 34 µm. The device in Figure 4.14 (a) is etched for 10 cycles of

DRIE and 40 cycles of XeF_2. The depth of Figure 4.14 (a) is inferred from a device that received the same processing conditions, had the mesh removed, and was measured with a Dektak profilometer. The device in Figure 4.14 (a) is kept intact and is etched for an additional 60 cycles of XeF_2 and is shown in Figure 4.14 (c). Here, the mesh bends more than in Figure 4.14 (a), but still touches the silicon which has a SHALLOW depth of 50 µm and a DEEP depth of 50.4 µm. The depth of the device in Figure 4.14 (c) is inferred from measurements of the corresponding 500 µm diameter open pit which has a SHALLOW depth of 53 µm and a DEEP depth of 53.4 µm. Figure 4.14 (b) is a close up image of (a) and the arrows point to the lip in the silicon between the DEEP and SHALLOW regions. Figure 4.14 (b) shows the mesh touching the silicon, but it is unclear in Figure 4.14 (d) if the mesh is contacting the silicon.

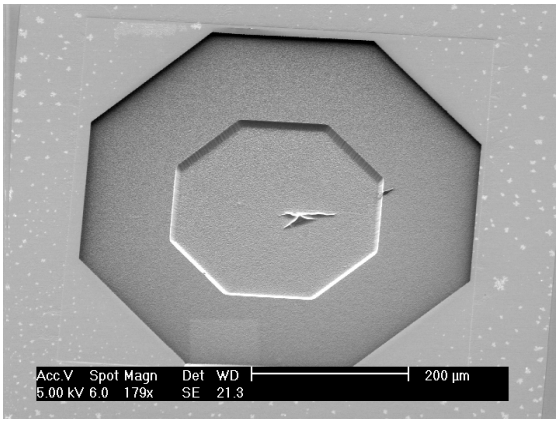

(a) outer SHALLOW depth of 10 µm
inner DEEP depth of 19 µm

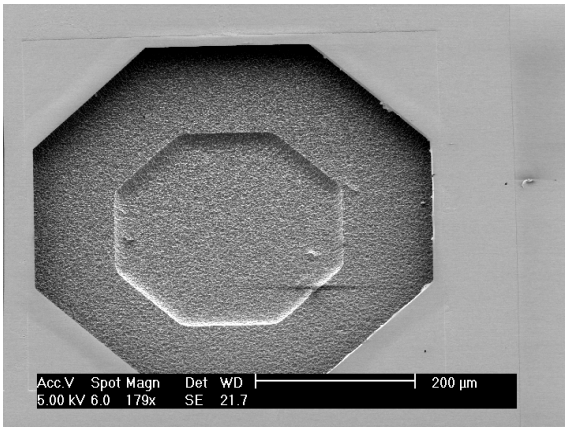

(b) outer SHALLOW depth of 30 µm
inner DEEP depth of 38 µm

Figure 4.15. SEM pictures of a 500 µm diameter open pits – fabricated without a mesh mask. Devices shown are from *Wafer K*.

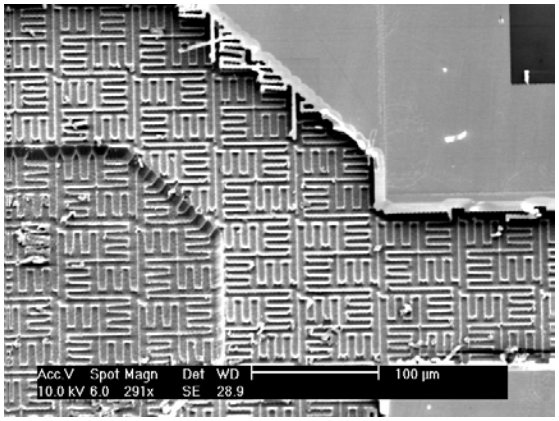

(a) outer SHALLOW depth of 10 µm
inner DEEP depth of 17 µm

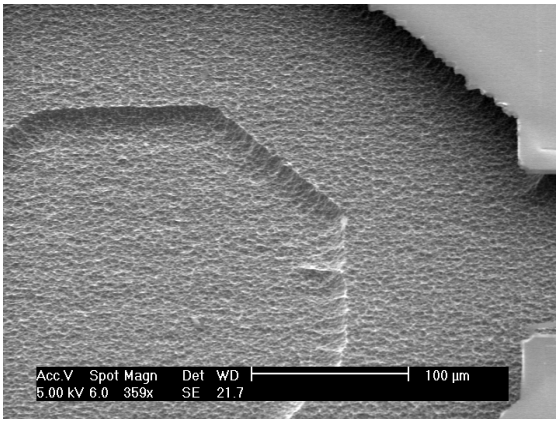

(b) outer SHALLOW depth of 28 µm
inner DEEP depth of 34 µm

Figure 4.16. SEM pictures of a 500 µm diameter mesh covered pits with the mesh removed.

Figure 4.15 shows the open etch pits used as a reference to gauge the depth of the mesh pits. Both pits are etched for 10 cycles of DRIE; (a) received 20 cycles of XeF_2 (b) received 40 cycles of XeF_2. Depth measurements are performed with a Dektak stylus profilometer. Figure 4.16 shows two MIXED 500 μm diameter pits which both received 10 cycles of DRIE. Figure 4.16 (a) has only been etched for 20 cycles of XeF_2 and the shadowing from the mesh is clearly visible. After 40 cycles of XeF_2 the shadowing has been wiped away as in Figure 4.16 (b).

4.3. Electrical Testing

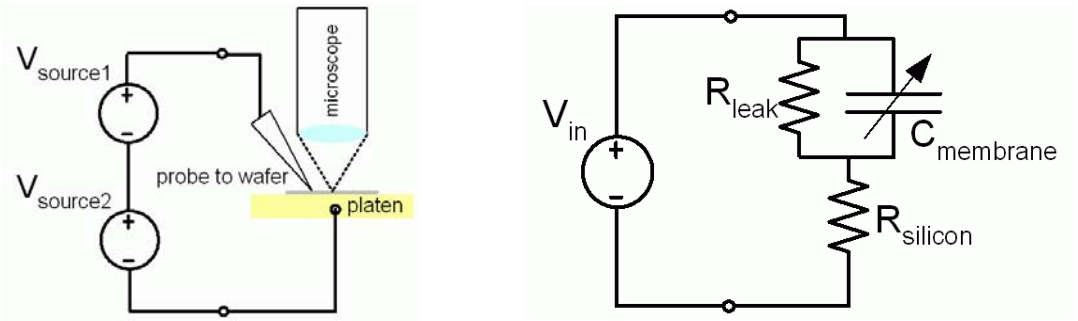

(a) Test setup schematic (b) Test setup circuit

Figure 4.17. (a) Two DC voltage supplies are connected in series with the devices. A Wentworth probe station allows deflection to be observed when a voltage is applied. (b) The circuit diagram of the test setup.

The device test setup is comprised of two voltage sources in series with the membranes, as shown schematically in Figure 4.17. In Figure 4.17 (b) a voltage is applied to the bond pad via a probe tip and a connection to the substrate via the platen. Electrostatic actuation is verified by observing movement under the microscope. Since the beams of the mesh are curved, only the flat parts of the mesh reflect light, the rest is dark. The reflected light on the beams moves when the mesh is successfully actuated.

A circuit diagram in Figure 4.17 (b) models the test set up. An input voltage, V_{in}, represents the two voltage sources. In the ideal case, the devices forms a perfect capacitor where the metal layer is always insulated from the silicon either by oxide or air. The capacitor is a variable capacitor because the membrane moves, hence the gap changes, with applied voltage. In practice, the metal touches the silicon at various points, either at holes in the oxide incurred during etching or where the released beams touch the bottoms of the silicon pits. The devices are modeled as a leakage resistance in parallel with a variable capacitor which is in series with the resistance of the silicon. Resistance and pull-in voltage are measured on the devices.

Table 4.18. Resistance in kΩ for membranes before XeF2 release. *(Wafer V)*

	500 μm	1000 μm	2000 μm
Deep	2.6	1.37	1.2
Mixed	1.94	1.49	1.06
Shallow	2.68	1.67	0.78

Table 4.19. Resistance in kΩ for membranes after 40 cycles of XeF2. *(Wafer V)*

	500 μm	1000 μm	2000 μm
Deep	2,600	1,370	1,200
Mixed	1,940	1,490	1,060
Shallow	2,680	1,670	780

Table 4.20. Resistance in kΩ for membranes after 8 cycles of XeF2. *(Wafer K)*

	500 μm	1000 μm	2000 μm
Deep	6.1	8.1	4.2
Mixed	7.9	7.2	7.5
Shallow	8.2	7.2	6.4

Table 4.21. Resistance data in kΩ for membranes after 48 cycles of XeF2. *(Wafer K)*

	500 μm	1000 μm	2000 μm
Deep	1,800	1,460	1,070
Mixed	1,700	1,360	830
Shallow	1,700	1,320	860

.

Table 4.22. Resistance data for membranes where the silicon has been etched to a depth of 2 μm SHALLOW and 10 μm DEEP. (From *Wafer K*)

	1000 μm	2000 μm
DEEP	3.5 kΩ	32 kΩ
SHALLOW	17.4 kΩ	3.8 kΩ

Table 4.23. Pull-in voltage data for membranes where the silicon has been etched to a depth of 2 μm SHALLOW and 10 μm DEEP. (From *Wafer K*)

	1000 μm	2000 μm
DEEP	46.8 V	>92 V
SHALLOW	26 V	24.8 V

Tables 4.18 and 4.19 show the difference in resistance before and after the isotropic etch on *Wafer V* to release the platinum from the silicon. At first the platinum is in contact with the silicon, thus there is a large surface area and low resistance. After 40 cycles, the contact area is greatly reduced, increasing the resistance.

The results for *Wafer V* are similar to the results shown for *Wafer K* in Table 4.20 and Table 4.21. The wafer was initially released from the silicon by 2.5 μm. Similarly, etching the silicon reduced the contact area and increased the resistance.

Table 4.22 and Table 4.23 show the data for one of the few wafers with actuating membranes. This data comes from devices with a relatively shallow etch – the resistance values are still quite low. Devices with a deeper etch and resistance in the MΩ range had actuating voltages >92 V, the maximum possible voltage given the test setup.

To test the effect of the hydraulic oil, a membrane was actuated with and without oil. In both cases the pull-in voltage was around 40 V. The difference with the oil was that the mesh popped back more slowly – taking a few seconds as opposed to around a second.

5. Conclusion

Researchers at Carnegie Mellon are collaborating to design and fabricate a fuel cell which will use a microfluidic pump based on the findings of this work. In this report preliminary theory, design, and fabrication are outlined for an actuated membrane which is a key component of the micropump. This project specifically set out to prove two concepts for micropump operation: zipper actuation and hydraulic coupling.

Equations governing theoretical operation of the membrane predict the relationship between applied voltage and pull-in radius with its resulting volume displacement. Most of the equations are taken from established sources; however, the equation relating membrane tension to electrostatic pressure is inferred and has not been proven. Another unproven assumption is that the membrane behaves as a membrane and not as a plate under large deflection. Further, not all of the values input to the equation are accurately known. Effective Young's modulus for the sealed mesh needs to be accurately determined. The Young's modulus used is for a membrane with a mesh made in CMOS-MEMS. Therefore, the results from the theory are a good first attempt, but still contain many areas that require validation and follow-up work.

Despite much effort in determining a suitable fabrication process, the platinum mesh beams still curled severely enough to render the devices inoperable. In all of the test devices, the curl of the beams warped the shape of the mesh and in many cases the beams touch the silicon. For the few devices that gave results, those results are not comparable with theory because the test devices do not correspond to their theoretical counterparts.

Suggestions are offered here which will help lead to more success in the future. Future work must reduce the curl in the beams. In the Simsox process, two approaches to consider would be to change the geometry, make the beams thicker and stiffer, or to adjust the sputtering recipe to reduce the stress gradient. Another option would be to use another more established and controllable process. The platinum mesh and the composite membrane are complicated devices which need to be characterized to determine an equivalent Young's modulus. Experiments must also prove if the ratio between deflection and thickness warrants characterization as a membrane or as a plate.

Ultimately, the device is so complicated that only numerical simulation will provide a truly reliable theoretical comparison.

Before any more work is done on fabrication, the theory must provide operational feasibility. The initial first-order theory of the current design indicates that the valve must be actuated at around 500 V, which is unreasonable for operation because it is greater than the breakdown voltage and far above the maximum voltage the fuel cell can practically supply. A custom process was chosen for this work to facilitate fluidic interconnect. It would be better to advance the pump's development as far as possible in CMOS-MEMS, where there is a better chance of getting micromechanical materials with low-stress gradients and more consistent material properties.

Nonetheless, there are still many improvements for the current fabrication process. To limit the curl, the platinum can be made thicker so the beams will be stiffer to resist bending. An annealing step might also help relieve the stress gradient in the platinum. The platinum was sputtered with a machine used by other users with many different metals and sputtering conditions; using a sputtering machine dedicated to this process might provide more consistent results. The line width and spacing of the cells was based on a conservative estimate of the resolution of the mask making machine. Another mask with a finer mesh would suffer from less from the effects of curl due to the shortened maximum beam length.

Many microfluidic pumps in the literature have been built, so the goal set forth is certainly achievable. With the right approach and mindset, this work can also be successful.

APPENDIX A: GLOSSARY OF ACRONYMS

ARDE	Aspect-Ratio Dependent Etching
CMOS	Complimentary Metal-Oxide-Silicon
DEEP	Refers to silicon patterned with both DRIE and XeF_2
DMFC	Direct Methanol Fuel Cell
DRIE	Deep reactive ion etching
I/O	Input/Output
MEMS	Microelectromechanical Systems
MIXED	Refers to silicon patterned with XeF_2 and selectively patterned with DRIE.
SEM	Scanning Electron Microscope
SHALLOW	Refers to silicon patterned with only XeF_2
Simsox	SIngle Metal Sing OXide fabrication technology
SOG	Spin-on glass
TSMC	Taiwan Semiconductor Manufacturing Company
BHF	Buffered hydrofluoric acid
DC	Direct Current
XeF_2	Xenon difluoride

APPENDIX B: GLOSSARY OF VARIABLES

dz/dt	Membrane velocity in the z-direction
E	Young's Modulus
$(EI)_{effective}$	Effective stiffness of a composite beam
F_B	Damping force applied to the membrane
g	Gap between electrodes
h	Thickness
I	Moment of inertia
L	Length
M	Moment
P_{elec}	Electrostatic pressure due to input voltage
P_{hydr}	Pressure of hydraulic fluid
R_i	Radial distance of master membrane pull-in
R_{max}	Radius of the membrane
S_{MASTER}	Tension per unit length caused by the stretching of the master membrane; units of N/m
S_{SLAVE}	Tension per unit length caused by the stretching of the slave membrane; units of N/m
V_{in}	Applied input voltage between the membrane and substrate
$V_{pull\text{-}in}$	The voltage at which the membrane snaps down to the substrate
W	Width
Z_{min}	Silicon pit depth
$Z_{SLAVE}(r)$	The shape of the slave membrane
α	A constant relating membrane thickness to the length of the membrane that contributes to electrostatic pressure
δ	Out-of-plane deflection
ΔU_{MASTER}	Volume displaced below the master membrane
ΔU_{SLAVE}	Volume displaced below the slave membrane
ε_0	Permittivity of vacuum
ε_r	Relative permittivity
ε_{r_strain}	Membrane strain
ν	Poisson's ratio
ρ	Radius of curvature
$1/\rho$	Curvature
σ	Material stress
μ	Dynamic viscosity

APPENDIX C: MASK LAYOUT

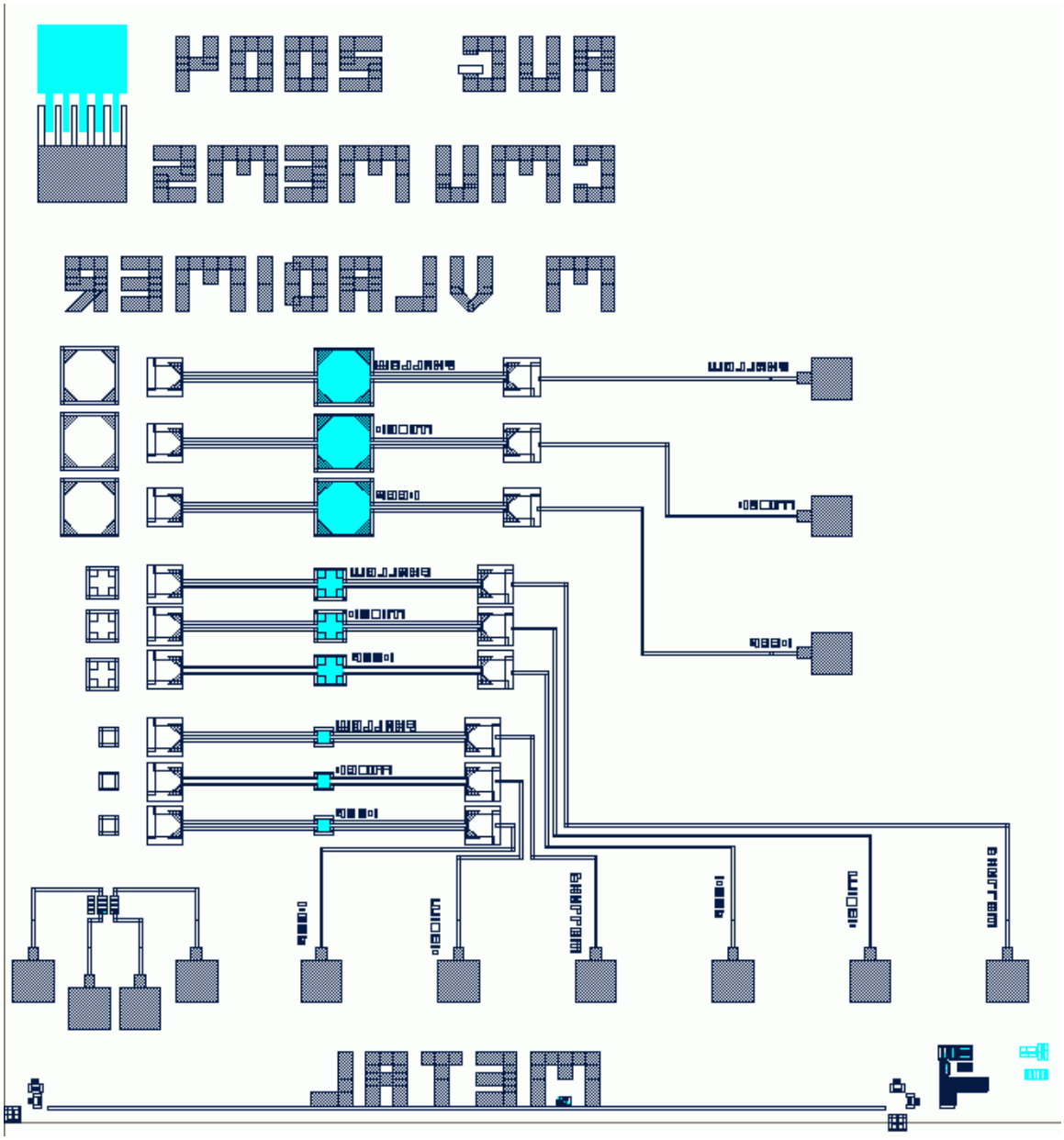

METAL MASK

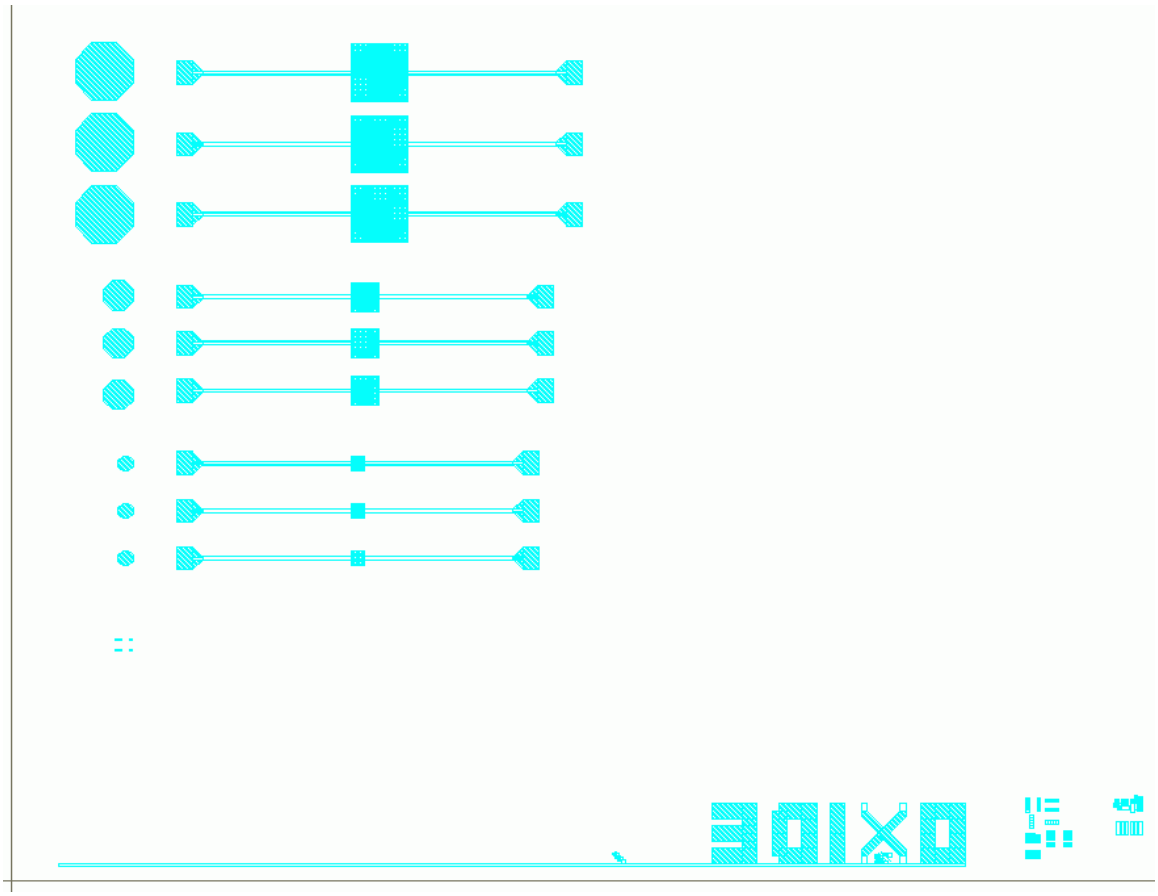

OXIDE MASK

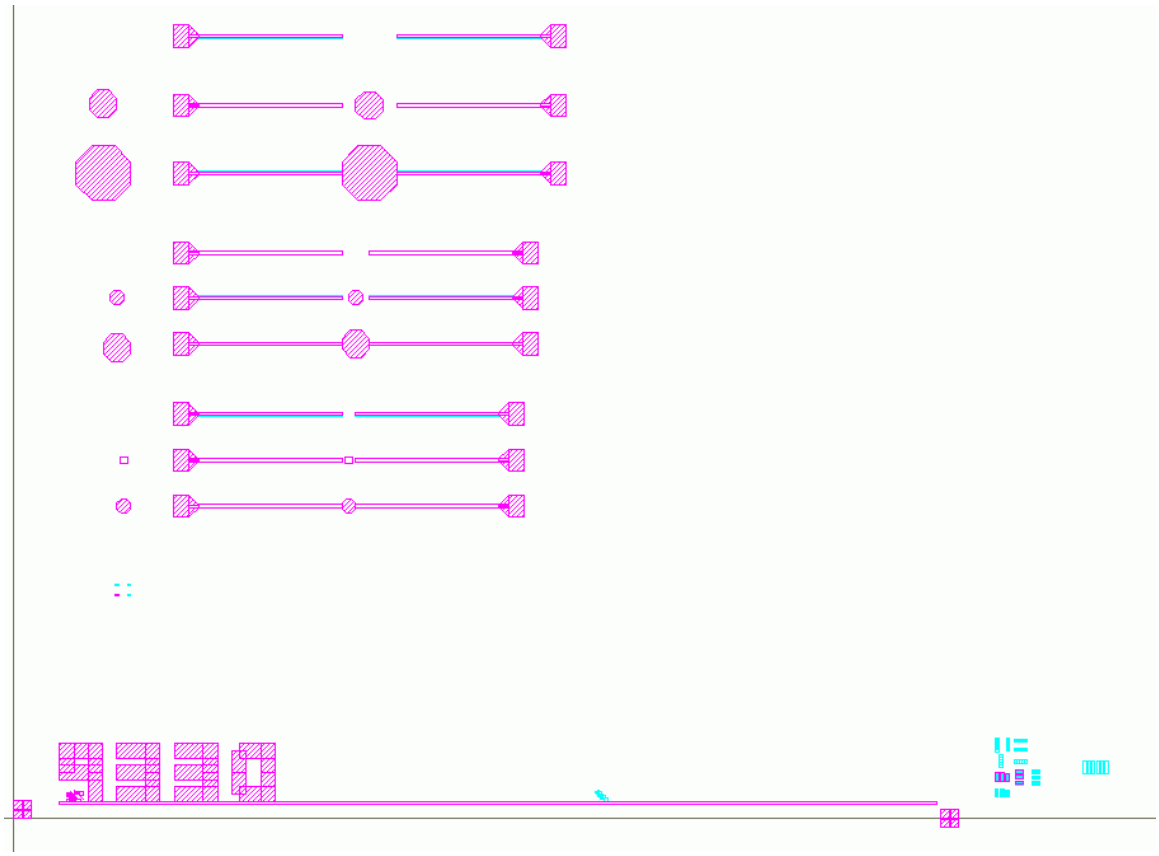

DEEP MASK

APPENDIX D: SIMSOX PROCESSS RECIPES

by Michael Vladimer based on George Lopez Subrebost's process

Mask Making

Times:	Convert design to .Lic files & transfer files	30 minutes
	Prep DWL (Warm up laser & load design)	20 minutes
	Run DWL	10-15 hours
	Finish DWL	5 minutes
	Make mask (develop photoresist, etch chrome, strip resist, clean up)	1 hour

Equipment:

- Heidelberg DWL (Direct Write Laser)
- Chem room solvent and acid wet benches
- two shallow trays
- Tweezers

Supplies:

- Chrome mask with photoresist AZ 1518
- AZ 400k developer
- Chrome etchant
- Acetone
- Propanol

1. Do designs in Cadence. ☺
2. If the design is smaller than ½ the wafer, put design on wafer multiple times to increase yield per wafer:

☺	☺
☺	☺

3. Load design in DWL
Mask note: Soda-Lime with chrome masks are low quality. If you heat the mask you risk cracking the chrome. Specifically, DO NOT PUT SOAD-LIME MASKS IN THE MASK WASHER IN THE CLEAN ROOM! The washer uses hot DI water and this caused the chrome on one of my masks to crack. (I'm pretty sure this was the cause.)
The reason for using Soda-Lime masks rather than Quartz is cost. Test soda-lime wafers cost $8.50/wafer; Prime soda-lime wafers cost $17/wafer; Quartz is $80/wafer.

4. Expose mask in DWL (my mask takes about 17 hours – which is the size of a full 4" wafer. If your design is smaller it'll be faster.)
DWL settings: 10% filter, 30% laser power sitting, 2047 defocus.
**Be sure to shut off Laser and vacuum after use!*

Due to the long exposure times, it's usually best to run the DWL overnight.

To develop:

This recipe is for Soda-Lime with chrome masks with AZ 1518 photoresist.

1. use 2 small plastic white trays: developer and stop-bath
2. Developer solution: Mix 1 part AZ 400k developer with 3 parts water. *I find 100ml:300ml works well for this.* Stir well to ensure good mixing.
3. Place mask in developer solution for 2 minutes. Immediately immerse in water stop-bath. Rinse for 1 minute with DI water gun and dry with N2.
4. take mask to microscope and inspect for photoresist residue. This will look like black streaks in the areas where the photoresist was removed.
   It's good to put a white tissue under the mask when you're loading it in the microscope. This is good to prevent scratching the glass and helpful when looking at the chrome etch.
   If you start to over etch, the photoresist will change color from red to green. This isn't necessarily a very bad thing since the over etched PR tends to hold up to the chrome etch quite well.
5. Once you're satisfied with the photoresist develop, put the developer solution waste in the 'Developer Waste' bottle and rinse clean both trays.
6. Fill one tray with chromium etchant, the other will be a water stop bath.
7. Put the mask in the chromium etchant for at least 90 seconds – I found 2 minutes works best. *The features will become clear after about 30 seconds. There is still chrome on the mask so keep etching!* Immediately immerse the mask in the water stop bath and rinse for 1 minute with DI water gun. Blow dry with N2.
8. Inspect the mask under the microscope to see if all the chromium is removed. *It helps to have a white tissue under the mask.*
9. Once you're satisfied with the chromium etch put the chromium etchant back in its bottle – it's reusable. Rinse clean the trays.
10. To remove the photoresist use acetone. I like to make 2 small baths: one of acetone, one of propanol. The photoresist tends to stick to the mask. Therefore, you need to scrub the mask with a swap. Cotton swabs work, but I prefer the foam swabs from the cleanroom. While the mask is in the acetone bath, rub it over with the swab. After the acetone bath, put the mask in the propanol bath. Blow dry with N2.
    If the mask doesn't look clean – i.e. there are dark and light patches on the chrome – that probably means there's still photoresist on it. You need to scrub with acetone.
11. The mask should be done. DO NOT RINSE/DRY WITH THE CLEANROOM WASHER!!! Do not heat the mask! The soda lime will expand and cause the chrome to crack.

Oxide Patterning: Photoresist Spinning

Times:	Pre-bake wafers and warm up hotplate	15 minutes
	Spin wafers	~30 minutes
	Expose wafers in Karl Suss	15 minutes
	Develop wafers	30 minutes

Equipment:

- Clean room spinner/vacuum hotplate
- 120 C oven
- shallow petri dish
- tweezers

Supplies

- Shipley 1813 photoresist
- Silicon wafers (with 1um grown Thermal Oxide)
- HMDS (hexadimethylsiloxane)
- 60mm droppers

1. Prep stuff:
    a. Set the vacuum hotplate to 115 C.
    b. Bake the wafers for 10 minutes in the 120 C oven.
    c. Spin recipe:
        i. 600 rpm at 5000rpm/sec for 6 seconds
        ii. 4000rpm at 5000/rpm/sec for 30 seconds
    d. Bake recipe at 115 C:
        i. Vacuum for 90 seconds
        ii. Proximity for 2 seconds
        I have the proximity step so that it lifts the wafer. Otherwise I find the wafer is still stuck to the hotplate and hard to get off.
    e. Use 'PROG' to load the programs into the spinner and hotplate. Right now the programs are under number '4'.
2. Let the wafers cool for 1 minute (until room temp).
3. Spin:
    a. load wafer in spinner
    b. Press 'START' to do a test spin to check if centered
    c. apply one dropper of HMDS
    d. press '0' to do another test spin.
    I find that helps to evenly coat the wafer.
    e. press 'START'. Let the wafer spin for the 6 second spread step then for 5 seconds let it spin. after about 2 seconds the color should stabilize. press 'STOP' to end the spin.
    f. Press 'START' to test spin again. *At this point the spinner is reset and must do another slow test spin before actually spinning. I find*

that the slow test spin is bad for photoresist spreading, so I do it before dispensing PR.

g. dispense a dropper of 1813.
I always use new droppers for application of photoresist to reduce the chance of putting particles on the wafer. I find it's ok to reuse the HMDS dropper, though.
h. press 'START' to spin. allow to spin for the whole program.

4. Bake:
   a. Press '***?***' to cycle from the spinner to the hotplate.
   b. Remove the wafer from the spinner. *Hold the wafer with tweezers and have the wafer ready to be placed on the hot plate*. Press 'START' then immediately put the wafer on the hotplate.
   c. Allow the wafer to cool for a minute, then expose and develop.
5. Expose:
   a. Open gas lines. Turn on Karl Suss. Press "Center" and "W/O Cass."
   b. In Karl Suss mask aligner load wafer and mask.
   c. Expose for 5 seconds for silicon wafer with 1um oxide.
   d. Turn off Karl Suss. Close PV and CA gas lines – leave N2 open to cool off the lamp.
6. Develop:
   a. Prep 2 small dishes: one wash bath of DI water, one developer bath of 1:1 Shipley Microposit Developer to DI water. I find 80ml:80ml works well. Don't use less than 125ml total.
   b. Develop for 2.5 minutes.
   c. Turn off N2 for Karl Suss.

Oxide Etching

Times:	HF etch	1 hour

At this point the wafer should be a 4" silicon wafer with 1um thermal oxide with a patterned layer of photoresist. The resist should expose the areas of the oxide that are to be removed.

Equipment:

- Delrin dishes
- Plastic wafer holder dip-stick things
- plastic tweezers
- safety equipment: face shield, apron, yellow gloves
  I usually buy new gloves for this because I don't want to risk getting gloves with holes.
- 1000ml plastic beaker
- Cleanroom rinser/dryer

Supplies

- Buffered Hydrofluoric Acid (BHF)
- Wafers patterned with oxide pattern in photoresist

1. Prep stuff:
    a. Make a sign 'Danger HF Etch' & let the people around you know you're working with HF.
    b. Inspect the wafers before etching to see if the PR patterning looks right.
    c. Fill the 1000ml with DI water – it will be a wash bath for the wafers.
    d. Set out the delrin dishes on the bench. Place 1 wafer in each dish.
    e. Set the timer for 25 minutes
    f. Put on the protective equipment (face shield, apron, gloves)
2. Pour enough BHF in each dish to cover the wafer with ~0.5-1cm of liquid.
3. Start timer.
4. Occasionally (every 5-10 minutes) lightly stir the BHF in the dishes to agitate. *The photoresist is not robust and tends to break off with some agitation – so don't over do it!*
5. After 15-20 minutes start checking the back side of the wafer for complete oxide removal. It's clear that the oxide is removed when the back of the surface changes from hydrophilic to hydrophobic – the backside will no longer look wet when you remove it from the BHF.
6. Once the backside is clear of oxide, wait an additional 1-2 minutes to insure full oxide removal on the front side.
7. Place the wafer holders close to the delrin dishes. *CAUTION! The wafers tend to stick to the bottom of the dishes. To remove them slowly and lightly lift the wafers. If you lift too hard the tweezers will slip on the wafers and splash HF!!!!!* Using the plastic tweezers transfer the wafers from the dishes to the holders.
8. Slide the locks on the holders down and rinse off the wafers for 60 seconds. Then place them in the 1000ml water bath for 60 seconds.
9. Blow one wafer dry and inspect under the microscope
10. Place the holders in the 50 C Kwik Strip bath. While the wafers are getting their PR stripped, clean up the acid bench. Rinse off all surfaces with DI water and blow dry with nitrogen.
11. Lightly agitate the wafers in the Kwik Strip bath. When the photoresist is removed, rinse the wafers off with DI water.
12. Clean the wafers in the rinser/dryer.

Metal Patterning: Spinning Photoresist

At this point the wafer should have a patterned layer of 1um thick thermal oxide. Next, the metal layer will be deposited through lift-off.
Pattern the photoresist the same way as for the Oxide Patterning, but with the Metal mask. Since the photoresist is on the same combination of layers—thermal oxide on silicon—the exposure time can remain unchanged.

Metal Sputtering

Times:	Prep samples and load Lesker	30 minutes
	Pump down Lesker	4-6 hours
	Run Lesker	30 minutes
	Unload Lesker	5 minutes

Now a layer of photoresist with the metal pattern is on the patterned oxide. A layer of metal – Platinum with Titanium cladding – is sputtered on using the Lesker in the Chem Room.

Equipment:

- Lesker Sputtering Machine
- Scissors

Supplies

- Wafers with patterned oxide and patterned photoresist
- Kapton Tape

1. Bring the Lesker to atmospheric pressure
2. Load the Titanium target in gun #2 and Platinum target in gun #1.
   Double check the guns – gun 2 has been having lots of problems lately.
3. Tape the 4" wafers to the mount
4. Pump down the Lesker (4-6 hours)
5. Sputter each wafer with 50A of titanium and 1000A of platinum
   a. Titanium for 20 seconds at 100W at 5 mTorr
   b. Platinum for 2.5 minutes at 75W at 20 mTorr
   **Remember to switch the DC power cable!*
   The purpose of the titanium is to facilitate lift-off by making the platinum sheet-like.
6. Unload wafers

Metal Lift-off

Times:	Wafer Soak	30 minutes
	Wafer ultrasonic	20 minutes
	Rinse and dry	15 minutes

The wafer is coated in Platinum over patterned photoresist. Below is patterned oxide. Remove photoresist and excess platinum with lift-off.

Equipment:

- Small glass dishes
- delrin dishes
- Cleanroom rinser/dryer

Supplies

- Platinum coated wafers with patterned oxide and patterned photoresist
- Acetone
- Acetone wash bottle, Propanol wash bottle, DI water gun

1. Soak the wafers in acetone for 30 minutes.
2. Rinse off with acetone
3. Put in ultrasonic with fresh acetone for 5 minutes
4. rinse again with acetone; rinse with propanol; rinse with DI water
5. Rinse and dry with rinser/dryer.

TESTING: Measure resistance

There is a short between the metal and the silicon. This resistance should increase as the contact area decreases during the bulk etching. Measure the resistance before and after to determine

Equipment:

- Wentworth probe station
- SEM
- Cleanroom rinser/dryer

Supplies

- Wafers with patterned oxide and metal

1. Measure Resistance.
2. SEM - take pictures of the devices to document changes.
3. Wash wafers with rinser/dryer to remove dust accumulated in ambient environment.

Deep Patterning: Spinning Photoresist

Now all the surface layers are on the wafer and patterned. The last step is to release the devices by bulk etching.

To create a two-tiered level in the silicon a protective photoresist mask is used to selectively etch the silicon. Then the mask is removed to etch all the silicon. Again, pattern the photoresist the same way as for the Oxide Patterning, but with the Deep mask. Since the photoresist is on the same combination of layers—thermal oxide on silicon—the exposure time can remain unchanged.

DRIE bulk silicon etching

Times:	DRIE etching in STS	30 minutes

Etch the silicon with DRIE to begin the 2-tiered silicon substrate with directional etch..

Equipment:

- STS etcher

Supplies

- Wafers with Deep patterned photoresist

1. Run the wafers on the Deep recipe for ??? cycles
   1 cycle = 1 – 1.5 um etch
2. Remove the wafers.
   At this point no more wet etching can occur. Do not blow N2 on the structures or they will be damaged!

Photoresist removal with PlasmaTherm

Times:	Oxygen plasma	20 minutes

Since wet etching is no longer an option, the Deep photoresist mask cannot be removed with acetone. Instead, it is removed with an oxygen plasma.

Equipment:
- PlasmaTherm etcher

Supplies
- Wafers with Deep patterned photoresist

1. Do oxygen clean 5 minutes at 200W

XeF_2 bulk silicon etching

Times:	XeF2 etching in XACTIX	30 minutes

Finish the 2-tiered silicon substrate profiling with isotropic XeF2 etch.

Equipment:
- XACTIX XeF2 etcher

Supplies
- Wafers with Deep patterned photoresist

1. Run the wafers for ??? cycles

TESTING: Measure resistance and Vpull-in

The devices are now released and will actuate. Find R and Vpull-in for each device.

Equipment:
- Wentworth probe station
- SEM

Supplies
- Wafers with patterned oxide and metal

1. Measure Resistance.
2. SEM - take pictures of the devices to document changes.

Sealing membranes: polymer deposition

Times:	Polymer deposition in STS	30 minutes

Using only the passivation cycle from the DRIE process, deposit polymer on the mesh to seal the membrane.

Equipment:

- STS etcher
- Kapton tape
- Scissors

Supplies

- Released wafers

1. Protect the bond pads with Kapton tape
   The polymer insulates and will make it very hard to probe the bond pads.
2. Run the wafers on the Polydep recipe for ??? minutes
   1 minute = ~0.15um of polymer
3. Polymer deposition – protect bond pads with kapton tape!!!!

BIBLIOGRAPHY

[1] Feynman, R. P., "There's Plenty of Room at the Bottom," – a talk given December 29th 1959 at the annual meeting of the American Physical Society at the California Institute of Technology (Caltech) First published in the February 1960 issue of Caltech's Engineering and Science.
On July 11, 2004 taken from http://www.zyvex.com/nanotech/feynman.html
Feynman, R. P., E. Hutchings, and R. Leighton, " 'Surely You're Joking, Mr. Feynman!': Adventures of a Curious Character," W. W. Norton & Company; Reprint edition (April 1, 1997) ISBN: 0393316041
The Feynman Lectures on Physics.

[2] Castaneda, C. "The Teachings of Don Juan: A Yaqui Way of Knowledge," University of California Press, Berkeley, California, p.24, 1968.

[3] Weintrob, N., S. Shalitin, and M. Phillip, "Why Pumps? Continuous Subcutaneous Insulin Infusion for Children and Adolescents with Type 1 Diabetes," Israel Medical Assoc. Journal, vol. 6, pp.271-274, May 2004.

[4] Mesa, J., A. Pérez, D. Figuerola, M. Fernandez Castañer, "Tratamiento con bombas de insulina," from Recomanacions cliniques Associació Catalana de Diabetis, 1999. Taken on July 11, 2004 from http://www.acdiabetis.org/acd/cas/html/protocolos.htm

[5] Yao, S. C., G. K. Fedder, X. Tang, C. C. Hsieh, Y. M. Alyousef, M. L. Vladimer, C. H. Amon, "Thermo-Fluids Considerations in the Development of a Silicon-based Micro-scale Direct Methanol Fuel Cell," Proceedings of The ASME – ZSIS International Thermal Science Seminar II. Bled, Slovenia, pp.171-180, June 13 – 16, 2004.

[6] Laser, D. J., and J. G. Santiago, "A review of micropumps," J. of Micromechanics and Microengineering vol. 14, pp.R35-R64, April 2004.

[7] Zengerle, R., A. Richter, and H. Sandmaier, "A micro membrane pump with electrostatic actuation," Micro Electro Mechanical Systems, 1992, MEMS '92, Proceedings. 'An Investigation of Micro Structures, Sensors, Actuators, Machines and Robot'. IEEE , 4-7 Feb. Pages: 19 -24, 1992.

[8] Judy, J. W., T. Tamagawa, and D. L. Polla, "Surface-machined micromechanical membrane pump" Micro Electro Mechanical Systems, 1991, MEMS '91, Proceedings. 'An Investigation of Micro Structures, Sensors, Actuators, Machines and Robots'. IEEE , 30 Jan.-2 Feb. 1991, Pages: 182 -186.

[9] Cabuz, C., W.R. Herb, E.I. Cabuz, Son Thai Lu, "The dual diaphragm pump" Micro Electro Mechanical Systems, 2001. MEMS 2001. The 14th IEEE International Conference on , 21-25 Jan 2001 Page(s): 519 -522

[10] Wagner, B., H. J. Quenzer, S. Hoerschelmann, T. Lisec, M. Juerss, "Bistable Microvalve with pneumatically coupled membranes" IEEE MEMS 1996, p. 384, 1996.

[11] van der Wijngaart, W., H. Ask, P. Enoksson, G. Stemme, "A high-stroke, high-pressure electrostatic actuator for valve applications" Sensors and Actuators A 100, p. 264-271, 2002.

[12] Saif, M. T. A., B. E. Alaca, and H. Sehitoglu, "Analytical Modeling of Electrostatic Membrane Actuator for Micro Pumps," J. MEMS, p. 335, Sept 1999.

[13] Kotera, H., M. Senga et al. "Optimization of thickness Distribution of Micro-Membrane by Genetic Algorithm." IEEE 1999.

[14] Mason, J. "MICRO FUEL CELLS HEADED TO MARKET, AND A SHOWDOWN" Small Times, May 27, 2004. Taken on July 11, 2004 from http://www.smalltimes.com/document_display.cfm?section_id=93&document_id=7971

[15] Medis Technologies Ltd. Taken on July 11, 2004 from http://www.medisel.com/products.asp?id=82#Intro

[16] MTI Micro Fuel Cells Inc. (MTI Micro), a subsidiary of Mechanical Technology Inc. (NASDAQ: MKTY). Taken on July 11, 2004 from http://www.mtimicrofuelcells.com/technology/differentiation.asp

[17] Timoshenko, S. P. and S. Woinowsky-Krieger, "Theory of Plates and Shells," Second Edition (Int'l Ed.), McGraw Hill, Inc, London, p. 400-404, 1959.

[18] Zeleznik, M. A. "Characterization of CMOS MEMS Membranes for Audio Acoustics," Master's Thesis, Electrical & Computer Engineering, Carnegie Mellon University, August 2003.

[19] Madou, M. J. "Fundamentals of Microfabrication – The Science of Miniaturization," Second Edition, CRC Press, New York, 2002.

[20] Fedder, G. K. and K. J. Gabriel. Lecture #14 slides for 18-414: Intro to MEMS. Provides equation for squeeze film damping, F_B.

[21] Engineeringtoolbox.com. Relationship between dynamic viscosity and kinematic viscosity. Taken on September 26th, 2004 from: http://www.engineeringtoolbox.com/21_412.html

[22] Convertit.com. Used in measurement conversions. Taken on September 26th, 2004 from: http://convertit.com/Go/ConvertIt/Measurement/Converter.ASP

[23] Xtronics. com. Value of dynamic viscosity of air was Air @ 18°C 0.018 2 cP. Taken on September 26th, 2004 from http://xtronics.com/reference/viscosity.htm

[24] Neumann, J. J., Jr., and K. J. Gabriel, CMOS-MEMS Membrane for Audio-Frequency Acoustic Actuation, in Technical Digest of the 14th IEEE International Conference on Micro Electro Mechanical Systems (MEMS 2001), Interlaken, Page 236-239, , January 21-25, 2001.

[25] Sze, S. M. "Semiconductor sensors," Wiley-Interscience Publications, New York, 1994.

[26] Nix, W. D. "Mechanical properties of thin films," Metallurgical Transactions A, Vol. 20A, p. 2217-2244, November 1989.

[27] Bourouina, T., T. Masuzawa, and H. Fujita, "The MEMSNAS Process Microloading Effect for Micromachining 3D Structures of Nearly All Shapes," JOURNAL OF MICROELECTROMECHANICAL SYSTEMS, VOL. 13, NO. 2, pp. 190-199, APRIL 2004.

[28] Stillman, J., "CMOS MEMS Resonant Mixer-Filters" Master's Thesis, Electrical & Computer Engineering, Carnegie Mellon University, p. 74, July 2003.

[29] Senturia, S. D. "Micorsystem Design," Kluwer Academic Publishers, Norwell, Massachussets, p. 134-135, p. 211-212, 2002.

[30] EnvironmentalChemistry.com. Young's Modulus for platinum taken on September 14, 2004 from http://environmentalchemistry.com/yogi/periodic/Pt.html#Physical

COMPANIES

[101] Gelest, Inc.
11 East Steel Rd.
Morrisville, PA 19067
http://www.gelest.com
Phone: (215) 547-1015
Silicone Oil type DMS-T05

[102] Filmtronics, Inc.
PO BOX 1521
Butler, PA 16003
http://www.filmtronics.com/
Phone: 724-352-3790
Fax: 724-352-1772
Spin-on Glass type SOG 31F

[103] Silicon Quest International, Inc.
1230 Memorex Drive
Santa Clara, CA 95050
http://www.siliconquest.com/
Phone: (408) 496-1000
Toll Free:(800) 959-3556
Fax: (408) 496-1133